SN2019dge: a Helium-rich Ultra-Stripped Envelope Supernova

Yuhan Yao [1] Kishalay De [1] Mansi M. Kasliwal [1] Anna Y. Q. Ho [1] Steve Schulze [2] Zhihui Li [1] S. R. Kulkarni [1]
Andrew Fruchter [3] David Rubin [4] C. Fremling [5] Daniel A. Perley [6] Eric C. Bellm [7] Rick Burruss,[8]
Michael Feeney,[8] Jim Fuller [9] Avishay Gal-Yam [2] V. Zach Golkhou [7,10] Matthew J. Graham [5] George Helou [11]
Thomas Kupfer [12] Frank J. Masci [11] Adam A.Miller [13,14] Russ R. Laher [11] Anthony L. Piro [15]
David L. Shupe [11] Roger Smith [8] Ben Rusholme [11] Jesper Sollerman [16] Maayane T. Soumagnac [17,2] and
Jeffry Zolkower[8]

[1] *Cahill Center for Astrophysics, California Institute of Technology, MC 249-17, 1200 E California Boulevard, Pasadena, CA 91125, USA*
[2] *Department of Particle Physics and Astrophysics, Weizmann Institute of Science, 234 Herzl Street, 76100 Rehovot, Israel*
[3] *Space Telescope Science Institute, 3700 San Martin Drive, Baltimore, MD 21218, USA*
[4] *Department of Physics and Astronomy, University of Hawai'i, 2680 Woodlawn Drive, Honolulu, HI 96822, USA*
[5] *Division of Physics, Mathematics, and Astronomy, California Institute of Technology, Pasadena, CA 91125, USA*
[6] *Astrophysics Research Institute, Liverpool John Moores University,*
IC2, Liverpool Science Park, 146 Brownlow Hill, Liverpool L3 5RF, UK
[7] *DIRAC Institute, Department of Astronomy, University of Washington, 3910 15th Avenue NE, Seattle, WA 98195, USA*
[8] *Caltech Optical Observatories, California Institute of Technology, Pasadena, CA 91125*
[9] *TAPIR, California Institute of Technology, MC 350-17, 1200 E California Boulevard, Pasadena, CA 91125, USA*
[10] *The eScience Institute, University of Washington, Seattle, WA 98195, USA*
[11] *IPAC, California Institute of Technology, 1200 E. California Blvd, Pasadena, CA 91125, USA*
[12] *Kavli Institute for Theoretical Physics, University of California, Santa Barbara, CA 93106, USA*
[13] *Center for Interdisciplinary Exploration and Research in Astrophysics (CIERA) and Department of Physics and Astronomy,*
Northwestern University, 1800 Sherman Road, Evanston, IL 60201, USA
[14] *The Adler Planetarium, Chicago, IL 60605, USA*
[15] *The Observatories of the Carnegie Institution for Science, 813 Santa Barbara St., Pasadena, CA 91101, USA*
[16] *The Oskar Klein Centre, Department of Astronomy, Stockholm University, AlbaNova, SE-10691 Stockholm, Sweden*
[17] *Lawrence Berkeley National Laboratory, 1 Cyclotron Road, Berkeley, CA 94720, USA*

Abstract

We present observations of ZTF18abfcmjw (SN2019dge), a helium-rich supernova with a fast-evolving (> 1 mag in 1 d) light curve indicating an extremely low ejecta mass ($\approx 0.3\,M_\odot$) and low kinetic energy ($\approx 1.2 \times 10^{50}$ erg). Early-time (< 4 d after explosion) photometry reveal evidence of shock cooling from an extended helium-rich envelope of $\sim 0.1\,M_\odot$ located at $\sim 3 \times 10^{12}$ cm from the progenitor. Early-time He II line emission suggests that the envelope might have a lower-density optically thin extension to 5×10^{13} cm. Subsequent spectra show signatures of interaction with helium-rich circumstellar material, which extends to $\sim 2 \times 10^{16}$ cm. We interpret SN2019dge as a helium-rich supernova from an ultra-stripped progenitor, which originates from a close binary system consisting of a mass-losing helium star and a compact object (i.e., a white dwarf, a neutron star, or a black hole). The remnants of 19dge-like ultra-stripped SNe are probably compact neutron star binaries, some of which can merge within the age of the Universe. We infer that the ratio of the rate of 19dge-like ultra-stripped SNe to core-collapse SNe is 2–12%, corresponding to a local rate density $R_{\rm dge}$ in the range of 1400–8200 Gpc^{-3} yr^{-1}. This provides an upper limit for the observed coalescence rate of compact neutron star binaries that are not formed by dynamical capture.

Keywords: supernovae: general – supernovae: individual (SN2019dge, iPTF14gqr) – stars: neutron

yyao@astro.caltech.edu

1. Introduction

Type Ibc supernovae (SNe Ibc) are believed to be explosions of massive stars that have lost their hydrogen

envelopes (Filippenko 1997; Gal-Yam 2017). Their typical rise times ($t_{\rm rise}$ in the range of 10–25 d) and peak luminosities ($M_{R,\rm peak}$ between -17 and -19 mag) suggest ejecta masses ($M_{\rm ej}$) of 1–5 $M_\odot$ and ^{56}Ni masses ($M_{\rm Ni}$) of 0.1–0.4 $M_\odot$ (Drout et al. 2011; Taddia et al. 2018; Prentice et al. 2019). The relatively low $M_{\rm ej}$ and high rates of SNe Ibc are not compatible with prediction from the evolution of single massive stars, whose mass-loss rates are not high enough to strip most of the outer layers (Smith et al. 2011; Lyman et al. 2016). In contrast, Wolf-Rayet (WR) or helium star descendants of massive stars in close binary systems are thought to be the dominant progenitors for the SN Ibc population (Dessart et al. 2012; Eldridge et al. 2013). The pre-SN star sheds its envelope by mass transfer to the companion, leaving a final envelope mass of 1 $M_\odot$ or more prior to explosion (Yoon et al. 2010).

SNe Ibc with the lowest $M_{\rm ej}$ arise from core-collapse of a stellar core with an envelope that was stripped to a greater extent. This can occur in tight binaries where a helium star transfers mass to a companion that is small in size. Such a scenario was invoked by Nomoto et al. (1994) as one way to explain the fast evolution of the Type Ic SN1994I with a carbon-oxygen progenitor star of $\sim 2\,M_\odot$ and $M_{\rm ej} \sim 0.9\,M_\odot$. Should the degree of stripping be even more extreme, we may expect the so-called *ultra-stripped* envelope SNe where $M_{\rm ej}$ and $M_{\rm Ni}$ are on the order of 0.1 $M_\odot$ and 0.01 $M_\odot$, respectively (Tauris et al. 2013, 2015; Suwa et al. 2015). These weak explosions are one of the two channels to form double neutron star (DNS) binaries that are compact enough to merge within a Hubble time due to gravitational wave (GW) radiation (Tauris et al. 2017)[1]. Ultra-stripped SNe are therefore a promising progenitor channel of multi-messenger sources that can be jointly studied by the LIGO/VIRGO network and electromagnetic efforts (Abbott et al. 2017a,b; Goldstein et al. 2017; Coulter et al. 2017; Hallinan et al. 2017; Kasliwal et al. 2017).

Compared with canonical SNe Ibc, we expect light curves of ultra-stripped SNe to be rapidly evolving and subluminous due to the small amount of $M_{\rm ej}$ and $M_{\rm Ni}$ produced. Among the group of faint and fast objects, SN2005ek (Drout et al. 2013), SN2010X (Kasliwal et al. 2010), as well as some of the calcium-rich gap transients such as PTF10iuv (Kasliwal et al. 2012), iPTF16hgs (De et al. 2018a), and SN2019ehk (Nakaoka et al. 2020) have been suggested to be good candidates for ultra-stripped SNe (Moriya et al. 2017). However, properties of these objects are also consistent with alternative interpretations, including core-collapse of stars with extended hydrogen-free envelopes (Kleiser & Kasen 2014; Kleiser et al. 2018a,b), and explosive detonation of a helium shell on the surface of white dwarfs (Shen et al. 2010; Sim et al. 2012; Polin et al. 2019; De et al. 2020a; Jacobson-Galán et al. 2020).

The most convincing ultra-stripped event to date is the Type Ic SN iPTF14gqr (De et al. 2018b). Its radioactivity-powered emission reveals $M_{\rm ej} \sim 0.2\,M_\odot$ and $M_{\rm Ni} \sim 0.05\,M_\odot$, whereas the detection of early-time shock cooling signatures shows that the progenitor is an extended massive star instead of a white dwarf, and therefore pins down its core-collapse origin. Discovered within one day of explosion, iPTF14gqr also demonstrated the importance of early-time observations in securely identifying ultra-stripped SNe.

Here we report the discovery, observations and modeling of the rapidly rising ($t_{\rm rise} \lesssim 3$ d) subluminous ($M_{r,\,\rm peak} \sim -16.3$ mag) helium-rich event ZTF18abfcmjw (SN2019dge) discovered by the Zwicky Transient Facility (ZTF; Bellm et al. 2019a; Graham et al. 2019). SN2019dge is consistent with being a helium-rich ultra-stripped SN. Section 2 describes the discovery and follow up observations. Section 3 outlines the basic properties of the explosion and its host galaxy. Section 4 shows modeling of the light curve and early-time spectra of this transient. Section 5 provides a discussion on the progenitor system, and Section 6 presents the estimated volumetric rates of 19dge-like ultra-stripped SNe. Section 7 gives a conclusion of this paper. Calculations in this paper assume a ΛCDM cosmology with $H_0 = 70\,{\rm km\,s^{-1}\,Mpc^{-1}}$, $\Omega_m = 0.27$ and $\Omega_\Lambda = 0.73$ (Komatsu et al. 2011). UT times are used throughout the paper. All spectra and photometry will be made available by the WISeREP repository (Yaron & Gal-Yam 2012) when the paper is accepted for publication.

2. Observations

2.1. Discovery

SN2019dge was discovered by ZTF, which runs on the Palomar Oschin Schmidt 48-inch (P48) telescope (Dekany et al. 2020). The first real-time alert (Patterson et al. 2019) was generated on 2019 Apr 7 10:18:46 (JD = 2458580.9297) for a g-band detection at 20.66 ± 0.34 mag and J2000 coordinates $\alpha = 17^{\rm h}36^{\rm m}46.75^{\rm s}$, $\delta = +50^{\rm d}32^{\rm m}52.2^{\rm s}$. On Apr 8, a new alert was flagged by a science program filter on the GROWTH Marshal (Kasliwal et al. 2019) that is designed to look for fast evolving transients.

---

[1] The other channel to form compact DNSs is dynamical capture in a dense stellar environment such as a globular cluster (East & Pretorius 2012; Andrews & Mandel 2019).
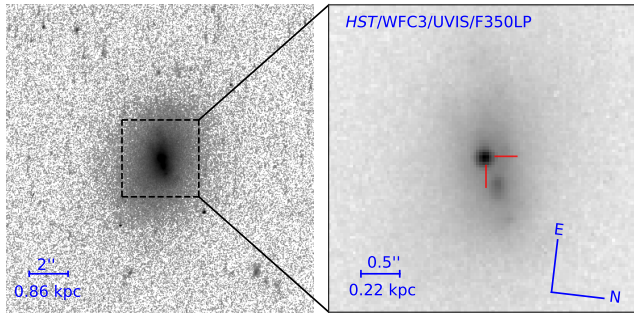
Figure 1. *HST* image of the field on Apr 22 in the F350LP filter at two intensity scales. The position of SN2019dge is marked by the red crosshairs in the right panel.

2.2. Follow-up Observations

2.2.1. HST Observation

Hubble Space Telescope (*HST*) observations were obtained as part of our *HST* "Rolling Snapshots" pilot experiment (GO-15675, Fruchter 2018). This new observational approach requires the PI to update a list of objects of interest each week before the schedule is built, giving the scheduler flexibility to choose a possible source for snapshots. Under this program, we obtained a NUV spectrum using the WFC3 G280 grism, a short (60 s) direct image of this field in the F300X filter to set the wavelength scale of the spectrum, as well as a longer exposure (200 s) in the F350LP filter. The image in the F350LP filter is shown in Figure 1. It has very similar throughput to the zeroth order of the G280 grism. We convolved this image to match the slight blurring of the zeroth order G280 grism and then scaled and subtracted it, dramatically reducing host contamination from the zeroth order host image.

SN2019dge resides in a compact galaxy SDSS J173646.73+503252.3. Our follow up spectra (see Section 3.2) suggest a host redshift of $z = 0.0213$, corresponding to a luminosity distance of $D_L = 93$ Mpc. As can be seen in Figure 1, there is a surface brightness peak in the northwest of SN2019dge (~ 0.2 kpc away), which might be the galaxy center. Since the explosion site is offset from the nucleus of the host, SN2019dge is unlikely to be associated with nuclear activity of any kind (AGN, TDE, etc).

2.2.2. Optical Photometry

Following Yao et al. (2019), we perform forced PSF photometry on ZTF difference images generated with the ZTF real-time reduction and image subtraction pipeline (Masci et al. 2019). ZTF image subtraction is based on the Zackay et al. (2016) image subtraction method. The sky region of SN2019dge is covered by two ZTF fields with fieldid (i.e., ZTF field identifier) 763

and 1799. We exclude all data in field 1799 since the reference image was constructed using images obtained between May 25 2018 and Jul 12 2019, which is after the explosion of the transient. Although the ZTF name of this object (ZTF18abfcmjw) may indicate that the transient was discovered in 2018, this is due to an alert generated on July 7 2018 from a candidate detection in negative subtraction (reference minus science) in field 763. We note that the seeing during that night was $4.2''$, larger than 99% of Palomar nights. The irregularly-shaped PSF might cause over-subtraction around the galaxy nucleus in the difference imaging process.

Since field 763 was included in both the northern sky survey with two epochs (one epoch each in g and r) per three nights and the extragalactic high-cadence survey with six epochs (three epochs each in g and r) per night (see Bellm et al. 2019b for the ZTF experiments design), SN2019dge was visited multiple times every night. Therefore, single-night flux measurements in the same filter are binned (by taking the inverse variance-weighted average). This gives a pre-explosion r-band limit of 18.95 mag (5σ limit computed at the expected position of the transient) on Apr 4 10:36:34. We convert 5σ detections to AB magnitudes for further analysis.

Following the discovery of SN2019dge, we obtained follow-up photometry in $griz$ with the optical imager (IO:O) on the Liverpool Telescope (LT; Steele et al. 2004). Digital image subtraction and photometry for LT imaging was performed using the Fremling Automated Pipeline (FPipe; Fremling et al. 2016). `Fpipe` performs calibration and host subtraction against Sloan Digital Sky Survey reference images and catalogs (SDSS, Alam et al. 2015).

LT and P48 photometry are shown in Figure 2. Absolute and apparent magnitudes are corrected for Galactic extinction $E(B-V) = 0.022$ mag (Schlafly & Finkbeiner 2011). We assume $R_V = 3.1$, and adopt thereddening law from Cardelli et al. (1989). We do not correct for host-galaxy contamination given the absence of Na I D absorption in all spectra at the host redshift. To estimate the epoch of maximum light, we interpolated the g- and r-band photometry with three-order polynomial functions, as shown in the inset of Figure 2. The time window used in the fit is from MJD = 58581.2 to 58585.2. SN2019dge was found to peak at $M_{g,\mathrm{peak}} = -16.45 \pm 0.03$ mag on MJD = 58583.19, and $M_{r,\mathrm{peak}} = -16.27 \pm 0.02$ mag on MJD = 58583.39. Hereafter we use phase (Δt) to denote time with respect to the g-band maximum light epoch, MJD = 58583.2.

We obtained one epoch of late-time imaging with the Wafer Scale Imager for Prime (WASP) mounted on the Palomar 200-inch telescope at ≈ 85 days from r-band
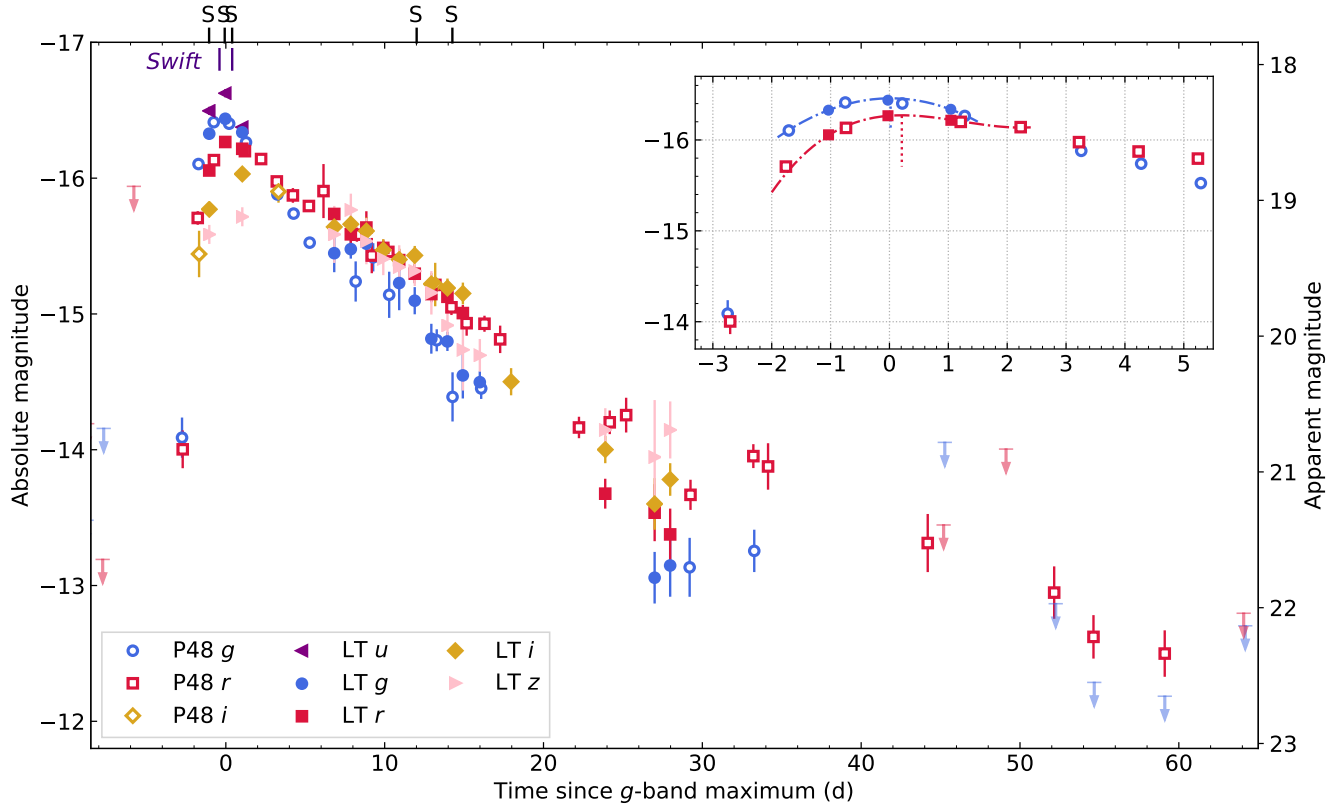
Figure 2. Galactic extinction corrected optical light curve of SN2019dge. The inset shows the light curve in g and r bands zoomed around the region of maximum light. Along the upper axis, epochs of spectroscopy are marked with the letter 'S' above of the axis, while two epochs of *Swift*/UVOT/XRT observations are marked below the axis.

peak. The data were obtained in r band with a total exposure time of $900\,\mathrm{s}$ divided into dithered exposures of $300\,\mathrm{s}$ each. The data were reduced using standard techniques as described in De et al. (2020b). Image subtraction was performed using archival reference images from the Dark Energy Legacy Survey (Dey et al. 2019), using the method described in De et al. (2020a). The median 5σ limiting magnitude of the image is $r \approx 25\,\mathrm{mag}$. However, the depth at the transient location is limited by the noise from the bright host galaxy, and the transient was not detected to a 5σ limiting magnitude of $r = 22.1\,\mathrm{mag}$.

We also performed forced photometry on archival PTF/iPTF difference images spanning May 07 2009 to Jun 13 2016 (Law et al. 2009; Rau et al. 2009). No historical detection was found.

2.2.3. Swift Observation

Space-based observations with the *Neil Gehrels Swift Observatory* (*Swift*; Gehrels et al. 2004) was triggered on Apr 9 and Apr 10. Ultraviolet/Optical Telescope (UVOT; Roming et al. 2005) data were obtained in the $UVW1$, $UVM2$, $UVW2$, U, B, and V filters.

UVOT data are reduced using `HEAsoft` (HEASARC 2014) version 6.17 with a $3''$ circular aperture. To remove host-galaxy contribution at the location of the SN, we obtained a final epoch in all broad-band filters on Jun 23 2019 and measured the photometry with the same aperture used for the transient. We present a table of our optical and UV photometry in Appendix A.

In parallel with the UVOT observations, *Swift* observed SN2019dge with its onboard X-ray telescope (XRT; Burrows et al. 2005) between 0.3 and $10\,\mathrm{keV}$ in the photon counting mode. We note that no point sources were detected in the XRT event files with SNR > 3. The 3σ limits (in $\mathrm{count\,s^{-1}}$) in the Apr 9, Apr 10, and Jun 23 observations are 7.8×10^{-3}, 5.8×10^{-3}, and 6.1×10^{-3}, respectively. To convert the upper limit count-rate to flux, we adopted the Galactic neutral-hydrogen column density of $N_\mathrm{H} = 2.89 \times 10^{20}\,\mathrm{cm^{-2}}$ towards SN2019dge (Willingale et al. 2013) and a power-law spectrum in the form of $N(E) \propto E^{-\alpha}$, where $N(E)$ has the unit of $\mathrm{photons\,cm^{-2}\,s^{-1}}$. We also assumed a flat spectrum with power-law index of $\alpha = 0.2$. Us-

Table 1. Log of SN2019dge spectroscopy.

Start Time	Instrument	Phase	Exposure Time	Airmass	Resolution (FWHM)
(UTC)		(day)	(s)		(Å)
2019 Apr 09 03:30:28	LT+SPRAT	−1.1	500	1.80	18
2019 Apr 10 03:06:10	LT+SPRAT	−0.1	500	1.80	18
2019 Apr 10 14:21:44	Keck1+LRIS	+0.4	300	1.17	6
2019 Apr 22 05:08:00	HST+WFC3+UVIS	+12.0	2×250	—	43
2019 Apr 24 11:06:43	P200+DBSP	+14.3	1200	1.05	3–5
2019 Jul 04 11:49:18	Keck1+LRIS	+85.3	1740	1.42	6
2019 Aug 31 08:04:58	Keck1+LRIS	+143.1	1150	1.41	6
2019 Sep 28 08:14:27	Keck1+LRIS	+171.1	600	2.17	6
2020 Feb 18 15:23:40	Keck1+LRIS	+314.4	1450	1.38	6

NOTE—Phase is measured relative to g-band maximum (MJD = 58583.2).

ing the PIMMS web tool[2], we obtained unabsorbed flux upper limits in the 0.3–10 keV band of 1.01, 0.75, and 0.79 $\times 10^{-12}$ erg s^{-1} cm^{-2}, corresponding to luminosities of 1.04, 0.77, and 0.81 $\times 10^{42}$ erg s^{-1}. We note that these limits are shallower than X-ray luminosities expected to be seen in SNe (Ofek et al. 2013b).

2.2.4. Radio Follow-up

Shortly after the discovery of SN2019dge, we initiated radio follow-up observations in order to constrain the presence of a radio counterpart, as potentially expected in some rapid-rising transients with circumstellar interaction (Weiler et al. 2007; Horesh et al. 2013; Ho et al. 2019a). We observed at high frequency radio bands using the Submillimeter Array (SMA, Ho et al. 2004) on UT 2019 Apr 09 between 15:49:17 and 19:51:26 UTC under its target-of-opportunity program. The project ID is 2018B-S047 (PI: Anna Ho). We did not detect SN2019dge in the resulting image, and the 3σ upper limits are 2.25 mJy at 230 GHz and 8.4 mJy at 345 GHz.

2.2.5. Spectroscopy

We obtained eight optical spectroscopic follow-up observations of SN2019dge from −1.1 d to +314.4 d relative to g-band peak using the Rapid Acquisition of Transients (SPRAT; Piascik et al. 2014) on the Liverpool Telescope (LT), the Double Spectrograph (DBSP) on the 200-inch Hale telescope (Oke & Gunn 1982), and the Low Resolution Imaging Spectrograph (LRIS) on the Keck-I telescope (Oke et al. 1995). To extract the LT spectra, we use the automated SPRAT reduction

pipeline, which is a modification of the pipeline for FrodoSpec (Barnsley et al. 2012). The DBSP spectrum was reduced using a `PyRAF`-based reduction pipeline (Bellm & Sesar 2016). LRIS spectra were reduced and extracted using `Lpipe` (Perley 2019).

A log of our spectroscopic observations is given in Table 1. We present our sequence of spectra in Figure 6, Figure 7 and Figure 10.

2.3. Host Galaxy Photometry

To obtain archival photometry of the host galaxy, we retrieved science-ready images from the Sloan Digital Sky Survey data release (DR9) (SDSS; Ahn et al. 2012), the Panoramic Survey Telescope and Rapid Response System (Pan-STARRS, PS1) DR1 (Flewelling et al. 2016), the Two Micron All Sky Survey (2MASS; Skrutskie et al. 2006), and the unWISE images (Lang 2014) from the NEOWISE Reactivation Year-3 (Meisner et al. 2017). We augmented this data set with *Swift*/UVOT observations that extend our wavelength coverage to the UV. The photometry was extracted with the software package `LAMBDAR` (Lambda Adaptive Multi-Band Deblending Algorithm in R; Wright et al. 2016), to perform consistent photometry on images that are neither pixel nor seeing matched, and tools presented in Schulze et al. (in prep). The UVOT data were reduced in `HEAsoft` as described in Section 2.2.3. The measured host photometry is given in Appendix A.

3. Properties of the Explosion and its Host Galaxy

3.1. Light Curve Properties

3.1.1. Peak Luminosity, Rise and Decline Timescale

[2] https://heasarc.gsfc.nasa.gov/cgi-bin/Tools/w3pimms/w3pimms.pl
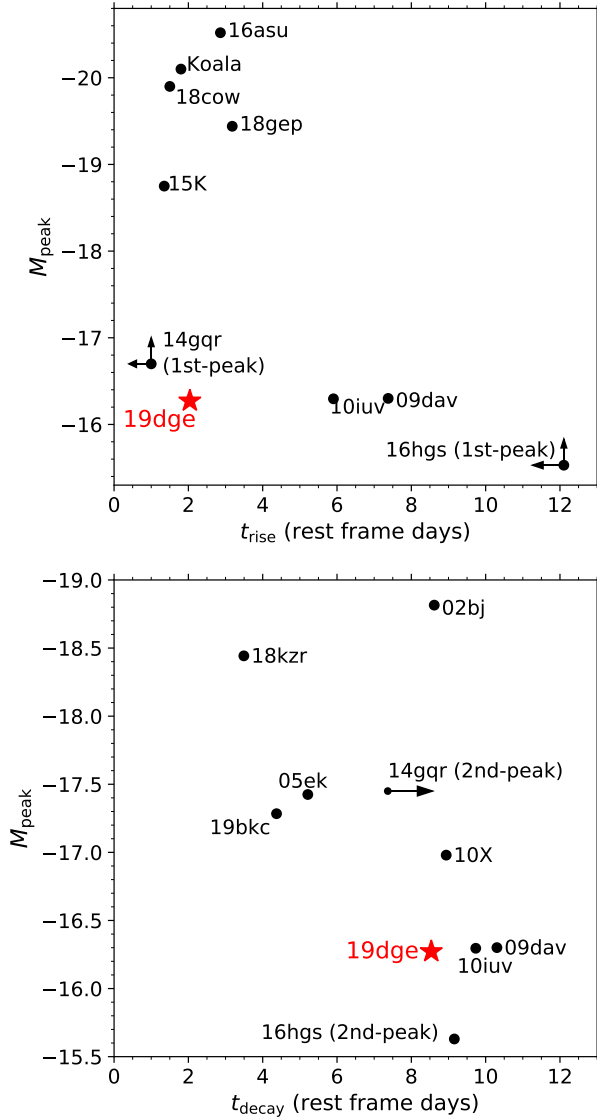
Figure 3. Comparison of the photometric evolution timescales ($t_{\rm rise}$ and $t_{\rm decay}$) and peak absolute magnitudes of SN2019dge (red asterisks) to other fast-evolving transients (black dots). See the text for details.

The g- and r-band peak luminosity of SN2019dge ($\approx -16.3\,$mag) is around the lower limit of stripped envelope SNe (Drout et al. 2011; Taddia et al. 2018; Prentice et al. 2019), and akin to those of the Ca-rich gap transients, which occupy the luminosity 'gap' between novae and SNe (peak absolute magnitude $M_R \approx -15.5$ to $-16.5\,$mag, Kasliwal et al. 2012).

To characterize the rise and decline timescales of SN2019dge, following Ho et al. (2020), we calculate rise time ($t_{\rm rise}$) defined by how long it takes the r-band light curve to rise from 0.75 mag below peak to peak, and decline time ($t_{\rm decay}$) determined by how long it takes to decline from peak by 0.75 mag (corresponding to half of maximum flux). Since SN2019dge shows no evidence of hydrogen (Section 3.2) and exhibits a fast rise (Figure 2), we compare the $t_{\rm rise}$, $t_{\rm decay}$, and peak absolute magnitude between SN2019dge and two other groups of transients:

- Fast-evolving hydrogen-deficient transients that are fainter than normal SNe Ia (i.e. $< -19\,$mag), including SN2002bj (Poznanski et al. 2010), SN2005ek (Drout et al. 2013), PTF09dav (Sullivan et al. 2011), SN2010X (Kasliwal et al. 2010), PTF10iuv (Kasliwal et al. 2012), iPTF14gqr (De et al. 2018b), iPTF16hgs (De et al. 2018a), SN2018kzr (McBrien et al. 2019), and SN2019bkc (Chen et al. 2020).

- "Fast evolving luminous transients" (FELT, Rest et al. 2018) or "fast blue optical transients" (FBOT, Margutti et al. 2019). We select well-studied representative objects of this population, including KSN2015K (Rest et al. 2018), iPTF16asu (Whitesides et al. 2017), AT2018cow (Prentice et al. 2018; Perley et al. 2019), SN2018gep (Ho et al. 2019b), and ZTF18abvkwla (also known as the Koala, Ho et al. 2020).

In Figure 3, peak magnitudes are given in (observer-frame) r-band, except for KSN2015K where we only have observations in the *Kepler* white filter, and iPTF16asu where the rise was only caught in g band. We only correct for Galactic extinction to compute $M_{r,\rm peak}$ (assuming no host extinction). Note that iPTF14gqr and iPTF16hgs are SNe exhibiting double peaked light curves. Since the rise to first peak was not captured, an upper limit of $t_{\rm rise}$ is calculated by taking the time difference between the first r-band detection and the latest pre-discovery non-detection[3], and absolute magnitude of the first r-band detection is considered to be a fainter limit of $M_{r,\rm peak}$ (plotted in the upper panel). In the lower panel, since observations of iPTF14gqr do not extend to 0.75 mag below its second peak, we present a lower limit of its $t_{\rm decay}$.

It is clear from the upper panel of Figure 3 that SN2019dge rose faster than normal Ca-rich events such as PTF09dav and PTF10iuv. The $t_{\rm rise}$ of $\approx 2.0\,$d is similar to the population of FELTs/FBOTs, but SN2019dge is substantially fainter. In the subluminous regime, iPTF14gqr has $t_{\rm rise}$ comparable to SN2019dge, and its first peak has been postulated to be caused by the diffu-

---

[3] For the second peak, $t_{\rm rise} \sim 5\,$d for iPTF14gqr and $8 < t_{\rm rise} < 20\,$d for iPTF16hgs.

sion of shock-deposited energy out of an envelope around the progenitor star (De et al. 2018b).

The bottom panel of Figure 3 shows that $t_{\rm decay}$ of SN2019dge is longer than that for the most rapid-fading SNe Ibc, such as SN2005ek, SN2018kzr, and SN2019bkc. Its decay timescale is more similar to SN2002bj, SN2010X, the population of Ca-rich transients (PTF09dav, PTF10iuv, iPTF16hgs), and likely iPTF14gqr. It has been suggested that the latter group of events have radioactivity powered main peak with low mass of nickel ($M_{\rm Ni} \lesssim 0.1\,M_\odot$).

3.1.2. Bolometric Evolution
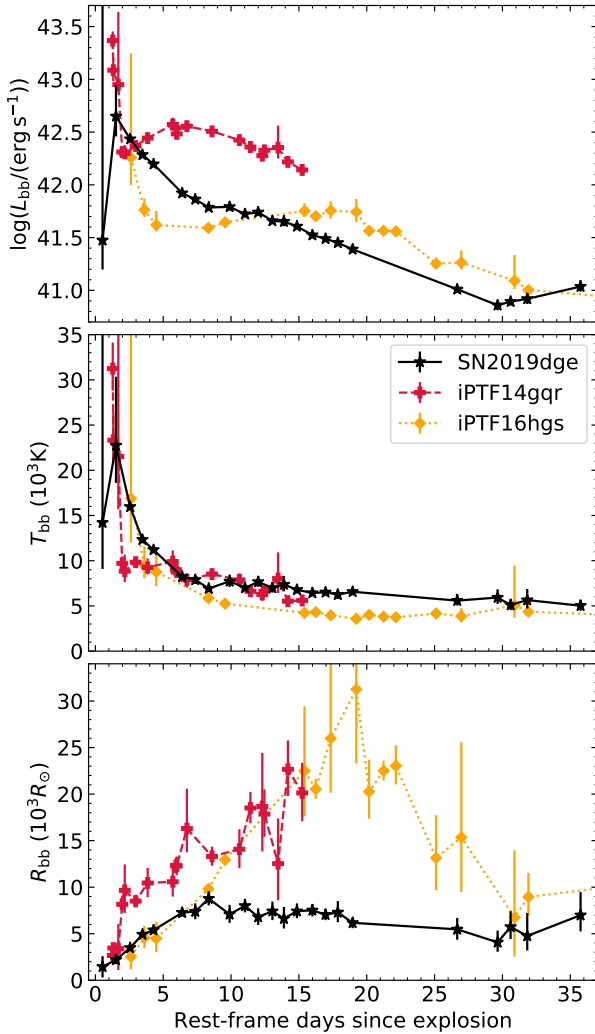
Figure 4. Evolution of blackbody properties (luminosity, temperature, radius) over time of SN2019dge compared to iPTF14gqr and iPTF16hgs. We use the same method as applied in SN2019dge to derive $L_{\rm bb}$, $T_{\rm bb}$, and $R_{\rm bb}$ for iPTF14gqr and iPTF16hgs.

We constructed the bolometric light curve at epochs where at least detections in two filters are available by fitting the spectral energy distribution (SED) with a blackbody function (see details of model fitting in Appendix B.1). We plot the physical evolution of SN2019dge with comparisons to iPTF14gqr and iPTF16hgs in Figure 4, where we have adopted the explosion epoch of iPTF14gqr, iPTF16hgs, and SN2019dge estimated by De et al. (2018b), De et al. (2018a), and Section 4.1 of this paper, respectively. The bolometric luminosity of SN2019dge reaches $\sim 5 \times 10^{42}\,{\rm erg\,s^{-1}}$ at $\sim 1.5\,{\rm d}$ after the explosion epoch. The subsequent decline displays an initial fast drop of $0.36\,{\rm mag\,d^{-1}}$ at age 2–9 d, and transitions to a slower drop of $0.11\,{\rm mag\,d^{-1}}$ at age 10–30 d.

The bolometric temperature of SN2019dge reaches as high as $\sim 2.3 \times 10^4\,{\rm K}$ at age 1.5 d and rapidly falls afterwards. The maximum $T_{\rm bb}$ is much hotter than that observed in normal SNe Ibc (6000–10000 K, Taddia et al. 2018). Its early light curve evolution is slower than iPTF14gqr, but similar to iPTF16hgs and several other stripped envelope SNe displaying double-peaked light curves (e.g., see Figure 2 of Fremling et al. 2019a). Their first peaks have been modelled by cooling emission from an extended envelope around the progenitor after the core-collapse SN (CCSN) shock breaks out (Modjaz et al. 2019). After $\sim 8\,{\rm d}$ past explosion, $T_{\rm bb}$ flattens to $6000 \pm 1000\,{\rm K}$, similar to the behavior of normal SNe Ibc at a much later phase ($\sim 30\,{\rm d}$ after explosion, Taddia et al. 2018).

Assuming that the photospheric radius can be approximated by $R_{\rm bb}$ and linearly expands at early phase, we fit a linear function to the first few $R_{\rm bb}$ vs. time measurements of SN2019dge which gives $\approx 8000\,{\rm km\,s^{-1}}$. The radius then remains flat at $\sim 6.7 \times 10^3\,R_\odot$ during age 8–30 d, and even appears to slowly recede. The reason for this is that the temperature drops to a recombination temperature for helium and the opacity becomes small. As a result, the outer layers of SN ejecta becomes more transparent, and deeper regions of the ejecta are being probed (Piro & Morozova 2014).

3.1.3. Color Evolution

We compare the color curves of other fast transients to that of SN2019dge in Figure 5, in corresponding pairs of $B/g - R/r$ and $R/r - I/i$ colors. For the double-peaked events iPTF14gqr and iPTF16hgs, "maximum" time corresponds to epoch of maximum light in the second peak.

The early-time blue color of SN2019dge arises from the high-temperature peak. Among other events, SN2002bj, iPTF14gqr and iPTF16hgs exhibit early colors as blue as
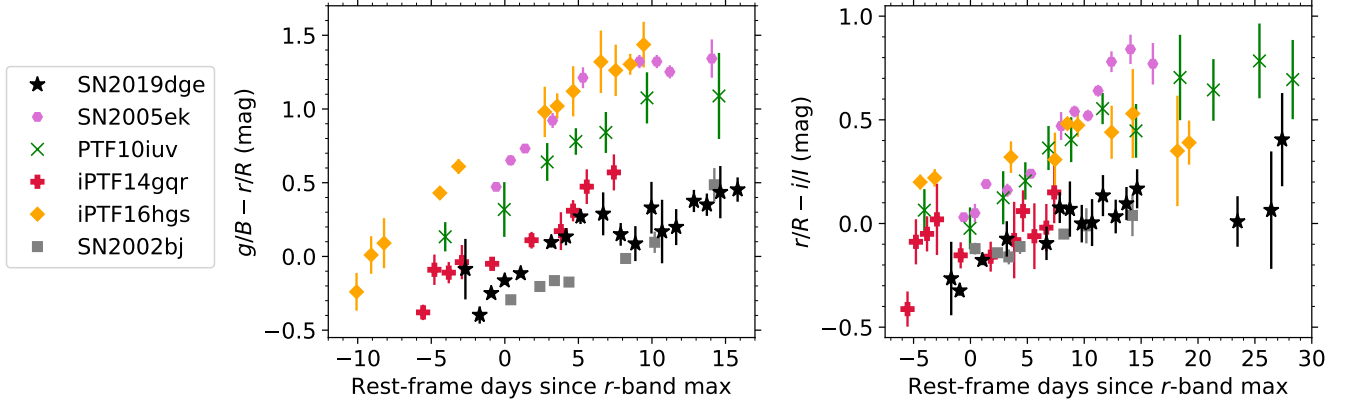
Figure 5. Comparison of the color evolution of SN2019dge with a subset of fast SNe shown in Figure 3. All colors have been corrected for Galactic extinction. Due to absence of photometry in identical filters, we compare colors in corresponding filter pairs of B/g, R/r and I/i. Since all SNe shown here are at relatively low redshifts ($z \leq 0.063$), the observed colors probe similar rest-frame bands.

SN2019dge. Subsequently, SN2019dge displays a color starting out blue and turning redder with time, consistent with a cooling process.

One unusual feature of SN2019dge is that at $\sim$ 6–9 d after maximum light, the $g - r$ color becomes bluer by ≈ 0.2 mag, while after that the color continues to redden. We notice that iPTF14gqr exhibits a similar trend — around 4 d before the second peak, its $g - r$ color stays flat before getting redder afterwards, while around 2 d before the second peak, its $r - i$ color also turns bluer by ≈ 0.2 mag.

3.2. Spectroscopic Properties

Table 2. Rest-frame FWHM ($\mathrm{km\,s^{-1}}$) of narrow emission lines in the +0.4 d, +85.3 d and +314.4 d LRIS spectra.

Transition	+0.4 d	+85.3 d	+314.4 d
He II $\lambda4686$	552 ± 36	—	—
He I $\lambda5876$	582 ± 86	272 ± 19	298 ± 24
He I $\lambda6678$	—	282 ± 28	339 ± 59
He I $\lambda7065$	—	230 ± 37	218 ± 26
Hα	291 ± 49	263 ± 13	280 ± 14
[S II] $\lambda6716$	285 ± 52	254 ± 14	274 ± 18
[S II] $\lambda6731$	263 ± 78	251 ± 14	264 ± 15
[O I] $\lambda6300$	—	263 ± 28	231 ± 24

3.2.1. Early Spectral Evolution

The very early spectra at -1.1, -0.1, and $+0.4$ d show a blue continuum and strong galaxy emission lines from the underlying H II region (see Figure 6). In addition, these spectra also show prominent He I $\lambda5876$ and high-ionization He II $\lambda4686$ narrow emission lines. We computed the equivalent width (EW) of He II emission using the spectral line and continuum wavelength ranges given by Khazov et al. (2016). The EW is found to be -7.56 ± 1.07 Å, -2.66 ± 1.30 Å, and -3.77 ± 0.16 Å in the -1.1 d, -0.1 d, and $+0.4$ d spectra.

In Table 2, we show the measured full width at half-maximum intensity (FWHM) velocities of some emission lines by fitting a Gaussian to the line profile. Since the [S II] $\lambda\lambda6716, 6731$ doublet is definitely from the host galaxy, their line widths serve as a practical measurement of instrumental line-broadening. As shown in column 2, FWHM velocities of the He II and He I emission lines are $\sim 550\,\mathrm{km\,s^{-1}}$ and $\sim 580\,\mathrm{km\,s^{-1}}$, much broader than the resolution of $\approx 270\,\mathrm{km\,s^{-1}}$, whereas H$\alpha$ is not well resolved. Thus, we infer that the hydrogen emission is from the host galaxy, while the helium lines are from photoionized material exterior to the SN.

3.2.2. Photospheric Phase Spectral Evolution

Broad transient features are present in the $+12.0$ and $+14.3$ d spectra (Figure 7). These spectra are taken at the photospheric phase where emission comes from a photosphere receding (in mass coordinates) back through freely expanding SN ejecta. The *HST* spectrum contains little host-galaxy contamination due to its high angular resolution. Prominent galaxy emission lines in the DBSP spectrum are identified and plotted in light red to emphasize transient features. The existence of the P-Cygni He I $\lambda5876$ profile and non-existence of hydrogen nominally classify SN2019dge as a Type Ib SN. We measure the velocity of the He I $\lambda5876$ line by fitting a parabola to the absorption minimum. The resulting
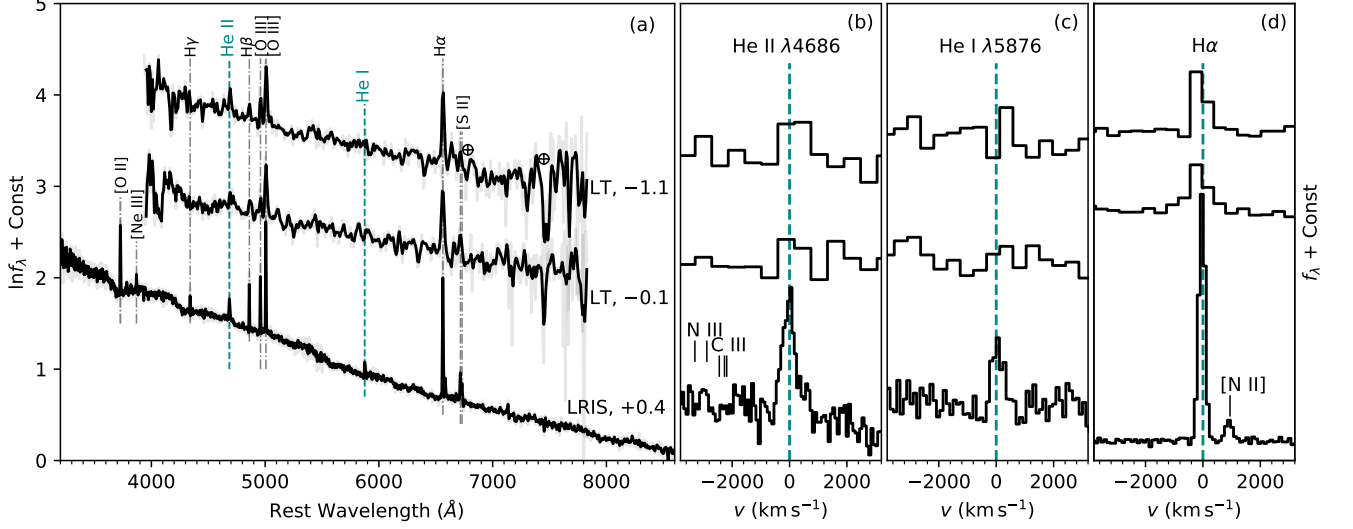
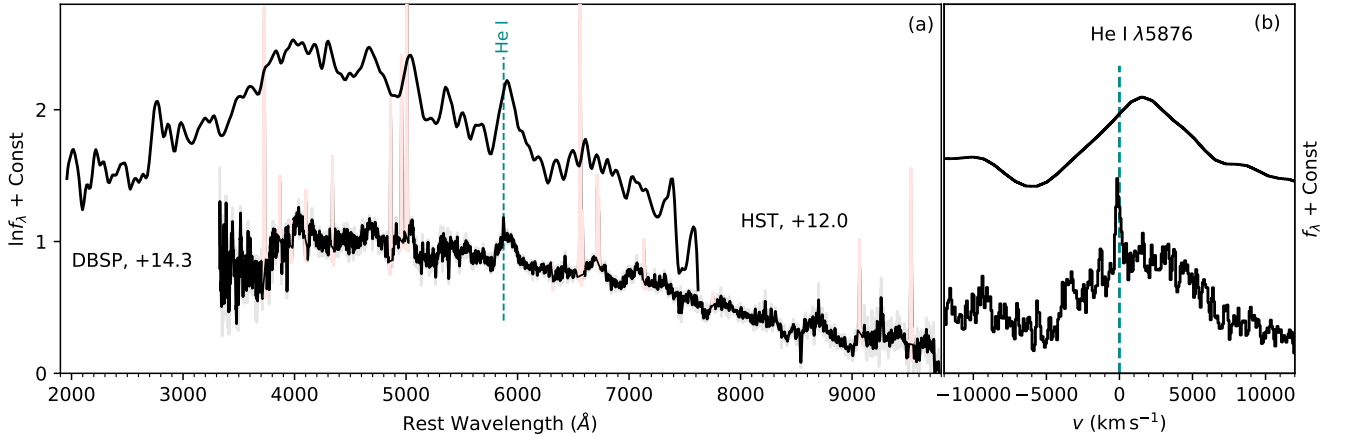**Figure 6.** Early-time spectra of SN2019dge. In panel (a), the original spectra are shown in translucent colors, with the overlying black lines showing the same spectra convolved with an FWHM $= 800\,\mathrm{km\,s^{-1}}$ (for LT) or FWHM $= 200\,\mathrm{km\,s^{-1}}$ (for LRIS) Gaussian kernel. Prominent galaxy lines are marked by the dash-dotted lines. In panel (b) (c) and (d), we show the observed spectra (not convolved) in velocity space around the He II $\lambda4686$, He I $\lambda5876$ and Hα emission lines.

Figure 7. Photospheric phase spectra of SN2019dge. In panel (a), the original DBSP spectrum is shown in translucent colors, with the overlying black lines showing the same spectrum convolved with an FWHM $= 200\,\mathrm{km\,s^{-1}}$ Gaussian kernel. We mask prominent galaxy lines in the DBSP spectrum in light red. In panel (b), we show the observed spectra (not convolved with any kernels) in velocity space around He I $\lambda5876$.

fits give velocities of $\approx 6000\,\mathrm{km\,s^{-1}}$ and $5900\,\mathrm{km\,s^{-1}}$ for the $+12.0\,\mathrm{d}$ and $+14.3\,\mathrm{d}$ spectra, respectively. This is lower than velocities of normal SNe Ib measured from the He I $\lambda5876$ absorption minimum ($\sim 10^4\,\mathrm{km\,s^{-1}}$, Liu et al. 2016), but higher than that in Type Ibn SNe ($\sim 3000\,\mathrm{km\,s^{-1}}$, Hosseinzadeh et al. 2017).

In Figure 8, we compare the photospheric phase optical spectra of SN2019dge with other helium-rich events. Note that the DBSP spectrum has host emission lines masked. SN2019dge is different from normal helium-rich stripped envelope SNe Ib/IIb or SNe Ibn in the sense that its P-Cygni absorption minimum in the He I $\lambda5876$ line is weaker. The feature at $\sim 5000\,\text{Å}$ is often attributed to He I $\lambda5016$ and Fe II triplet $\lambda\lambda\lambda4924, 5018$, and 5169 (Liu et al. 2016). The shape of this feature in SN2019dge is similar to those in normal SNe Ib/IIb at much later phases ($\sim 20\,\mathrm{d}$ post maximum), indicating that the spectral evolution of SN2019dge is faster. The complex absorption profile at $\sim 4500\,\text{Å}$ has been identified as a blend of Fe II, Mg II $\lambda4481$ and He I $\lambda4472$ (Hamuy et al. 2002). In the DBSP spectrum, we detected O I $\lambda7774$ and broad Ca II at $\sim 8500\,\text{Å}$ (due to
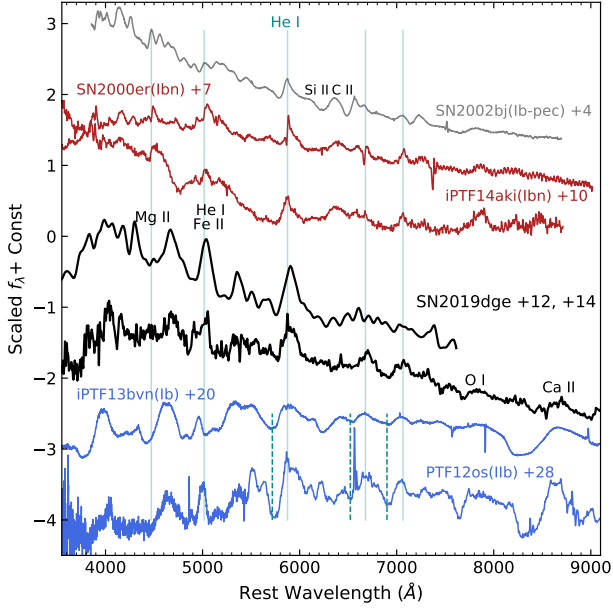
Figure 8. Photospheric phase spectra of SN2019dge compared with other SNe, including SN2000er (Pastorello et al. 2008), SN2002bj (Poznanski et al. 2010), iPTF14aki (Hosseinzadeh et al. 2017), PTF12os and iPTF13bvn (Fremling et al. 2016). He I transitions at rest wavelength are marked by the vertical cyan lines (though note that not all of these lines are visible in all spectra shown here).
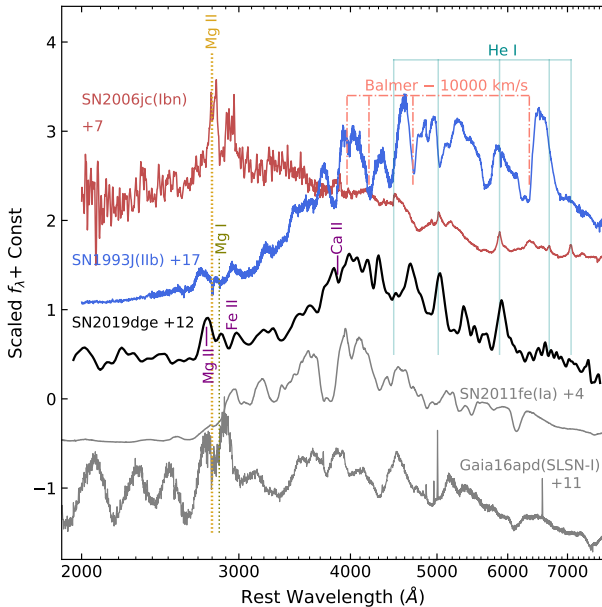

Figure 9. *HST* spectrum of SN2019dge compared with other SNe, including SN2006jc (Bufano et al. 2009), SN1993J (Jeffery et al. 1994), SN2011fe (Mazzali et al. 2014), and Gaia16apd (Yan et al. 2017).

the $\lambda\lambda$ 8498, 8542, and 8662 triplet) with clear P-Cygni profiles; Both are major features of stripped envelope SNe (Gal-Yam 2017).

In Figure 9, we compare the *HST* NUV spectrum with spectra of other types of SNe. The UV part of SN2019dge is much weaker than a blackbody extrapolation of the optical spectra would predict. This has also been seen in normal thermonuclear and CCSNe, and interpreted as strong metal-line blanketing caused by iron-peak elements, particularly Fe II and Co II (Gal-Yam et al. 2008). SN2019dge bears a close resemblance to SN1993J between 2000 and 4000 Å. In Figure 9, we also marked the rest wavelength of Mg I λ2852 and Mg II $\lambda\lambda$2796, 2803. The emission features at ~ 2760 Å in SN2019dge and Gaia16apd are similar to the bump at ~ 2730 Å in SN1993J, which was found to be a NLTE Mg II emission line (Jeffery et al. 1994). This resonance line is blueshifted from its rest wavelength, and is suggested to come from a circumstellar region that is distinctly separated from the SN photosphere in velocity and excitation conditions (Panagia et al. 1980; Fransson et al. 1984).

3.2.3. Late-time Spectral Evolution

Figure 10 shows late time spectra of SN2019dge obtained at +85.3, +143.1, +171.1, and +314.4 d. The general shape of the spectra is determined by the host galaxy, while possible SN features are marked by the dashed lines. The right panels (b), (c), and (d) highlight emission lines at wavelengths of He I, [O I], and [Ca II]. In panel (c) of Figure 10, the [O I] $\lambda\lambda$6300, 6363 feature consists of two narrow emission peaks. This doublet transitions share the same upper level ($^{3}P_{1,2}$–$^{1}D_{2}$). The observed intensity ratio $R \equiv F(6300/6364) \sim 3.1$ agrees with the nebular condition, as one would expect in the optically thin regime (Leibundgut et al. 1991; Li & McCray 1992). In panel (d), we mark the position of the [Ca II] doublet in dashed lines, but only the λ7324 line is clearly detected. It presents a double-peaked profile with a peak separation of $\sim 400 \, \mathrm{km \, s^{-1}}$.

From panel (a) of Figure 10, it is also clear that in the +85.3 d spectrum, the He I and [Ca II] lines have broader emission components with Lorentzian profiles at the bases of the narrow emission lines. These Lorentz-shape components are not visible in the +314.4 d spectrum. Therefore, to further investigate the broader features, we subtract the +314.4 d spectrum from the +85.3 d spectrum. The resulting subtraction (Figure 11) reveals intermediate-width (FWHM $\sim 2000 \, \mathrm{km \, s^{-1}}$) components of He I, [Ca II], and the Ca II IR triplet. It shares a close resemblance to some Type Ibn SNe, such as SN2011hw (Pastorello et al. 2015) and SN2015G
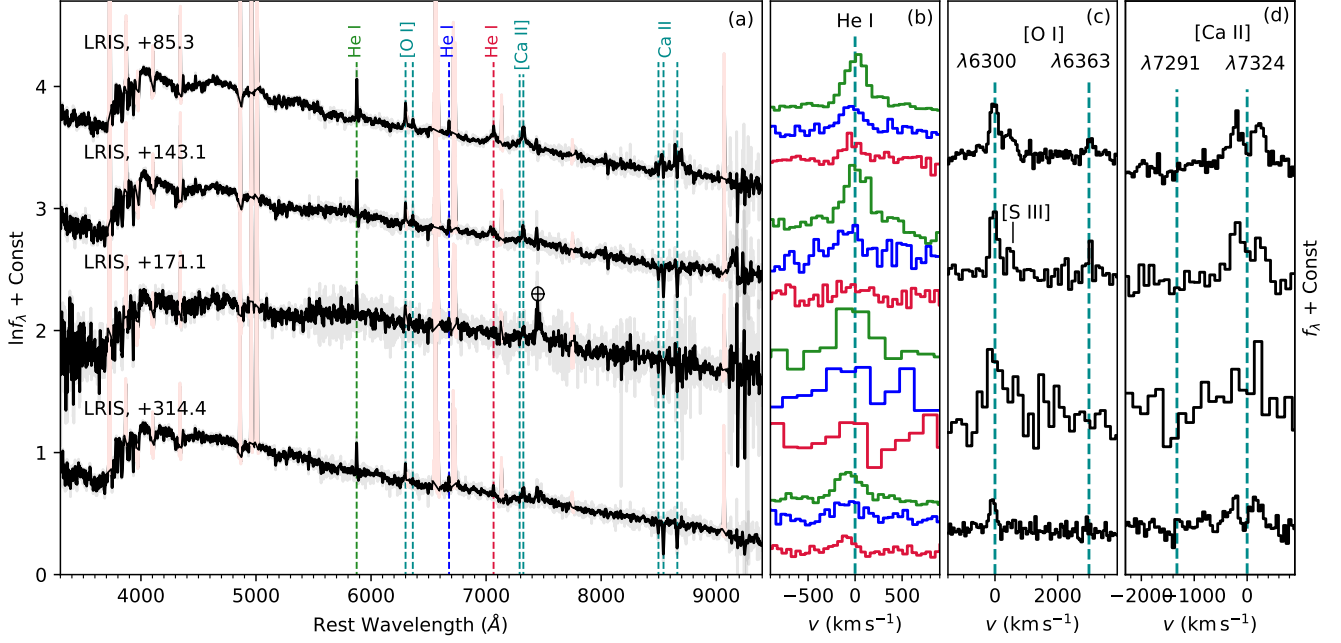
Figure 10. Late-time spectra of SN2019dge. In panel (a), the original spectra are shown in translucent colors, with the overlying black lines showing the same spectra convolved with FWHM = $200 \, \mathrm{km \, s^{-1}}$ Gaussian kernels. We mask prominent galaxy lines in light red. Possible SN features are marked by the dashed lines. In panel (b) (c) and (d), the spectra at phase +85.3 d, +143.1 d, +171.1 d, and +314.4 d, are binned by 1, 2, 3, and 1 pixel(s), respectively (1.16 Å per pixel). The binning factors are chosen based on the different signal-to-noise ratio (SNR) in these spectra (see exposure times in Table 1). Note that in panel (b), we plot evolution of He I $\lambda5876$, $\lambda6678$, and $\lambda7065$ emissions in green, blue, and crimson, respectively.

(Shivvers et al. 2017). These intermediate-width features are too narrow to be explained by emission from SN ejecta. Instead, they are probably emitted by a cold dense CSM shell formed by radiative cooling from the post-shock material, as has been proposed to be the case in interacting Type IIn/Ibn SNe (Chugai & Danziger 1994; Smith 2017).

Table 2 (column 3 and 4) gives the measured FWHM velocities of narrow emissions shown in panel (b), (c), and (d) of Figure 10. It can be seen that the measured FWHM of other emission lines are similar to the [S II] line-width. Therefore, we conclude that the observed narrow emissions are not resolved.

Due to the low resolution of our LRIS spectra, we cannot directly rule out the possibility that the narrow lines are emanating from the host galaxy. However, there are evidence indicating that they are not merely a background contamination of an underlying H II region:

(i) In the +85.3 d spectrum, the He I and [Ca II] narrow emissions are on top of intermediate-width Lorentzian components characteristic of electron scattering (Huang & Chevalier 2018), which fades away in the +314.4 d spectrum. However, the hydrogen Balmer lines do not have a broader base in any of our spectra.

(ii) The flux intensities of He I, [O I], and [Ca II] lines decrease by a factor of approximately two from +85.3 d to +314.4 d, consistent with the temporal evolution from an emission mechanism connected to the aging supernova. As a comparison, the line strengths of the strongest emissions in normal ionized nebulae ($H\alpha$, [O III], [O II], [S II], etc) do not follow this behavior.

(iii) Although the He I and [O I] lines labelled in panel (a) of Figure 10 have been observed in H II regions (Peimbert et al. 2000, 2017), the doublet [Ca II] $\lambda\lambda7291$, 7324 has not been detected in gaseous nebulae (Kingdon et al. 1995).

Taken together, we suggest that the narrow components ($\lesssim 270 \, \mathrm{km \, s^{-1}}$) of He I, [Ca II], [O I] and Ca II are also associated with the transient. Their widths might be consistent with the typical velocities of pre-shock CSM. The detection of these lines at $> 300 \, \mathrm{d}$ after the SN explosion suggests that the circumstellar shell extends to $\gtrsim 2 \times 10^{16} \, \mathrm{cm}$ ($\sim 1000 \, \mathrm{AU}$) from the progenitor.[4]

_____

[4] Adopting a conservative shock velocity estimation of $v_s \approx 10^4 \, \mathrm{km \, s^{-1}}$, the forward shock travels $2.6 \times 10^{16} \, \mathrm{cm}$ after 300 d.
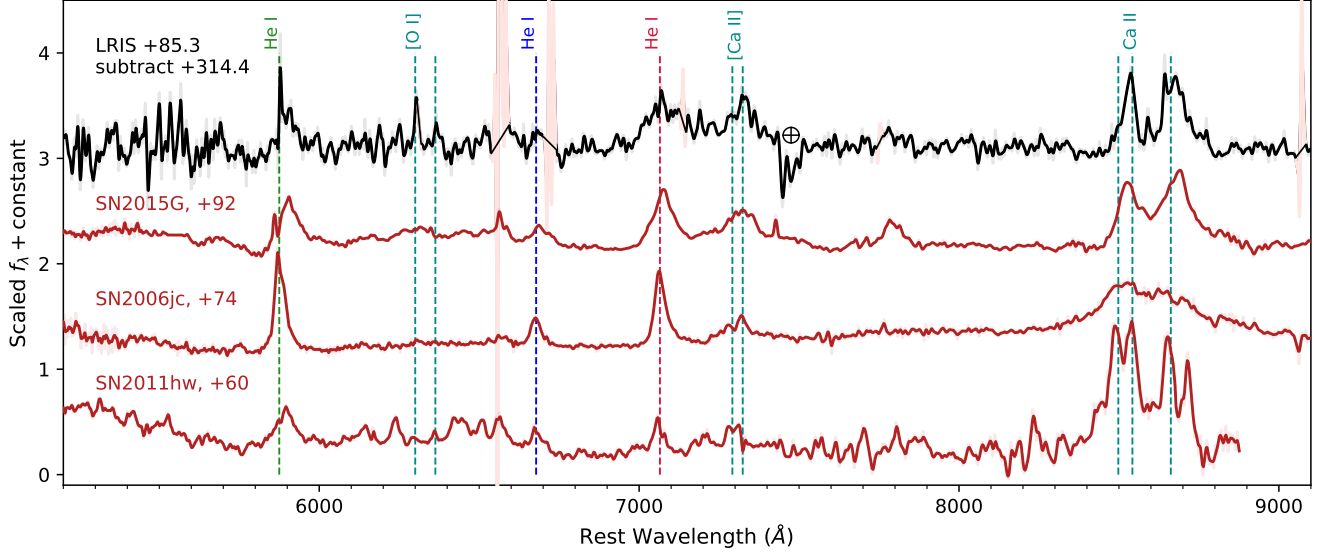
Figure 11. Subtracted late-time spectrum of SN2019dge compared with Type Ibn SNe SN2006jc (Shivvers et al. 2019), SN2011hw (Pastorello et al. 2015), and SN2015G (Shivvers et al. 2017).

3.3. Host Galaxy Properties

We measure properties of the host galaxy using the spectrum obtained at phase $+314.4\,$d, assuming that the most prominent nebular line emissions of Hα and [N II] are from the host. The Galactic extinction corrected emission line fluxes of Hα and [N II] $\lambda6584$ are $(24.15 \pm 0.54) \times 10^{-16}\,\mathrm{erg\,cm^{-2}\,s^{-1}}$ and $(1.92 \pm 0.10) \times 10^{-16}\,\mathrm{erg\,cm^{-2}\,s^{-1}}$, respectively. The fluxes were measured by fitting a Gaussian profile to the emission line profiles, measuring the integrated flux under the profile.

Using the Kennicutt (1998) relation converted to a Chabrier initial mass function (Chabrier 2003; Madau & Dickinson 2014), we infer a star-formation rate of $\approx 0.012 M_\odot\,\mathrm{yr}^{-1}$ from the Hα emission line. Note that this is a lower limit since the slit width in the LRIS spectrum is 1.0 arcsec ($\sim 0.44\,$kpc at the distance of the host) and the extraction aperture is 0.76 arcsec, whereas the host diameter is about 5 arcsec.

We also compute the oxygen abundance using the strong-line metallicity indicator N2 (Pettini & Pagel 2004) with the updated calibration reported in Marino et al. (2013). The oxygen abundance in the N2 scale is 8.23 ± 0.01 (stat) $\pm\,0.05$ (sys). We choose not to use the O3N2 index since it requires line flux measurement of Hβ. As can be seen in panel (a) Figure 10, there is substantial stellar absorption around Hβ ($4861\,$Å). Compared to $12 + \log(\mathrm{O/H})_{\mathrm{solar}} = 8.69$ (Asplund et al. 2009), the derived N2 index suggests a significantly subsolar metallicity of $\approx 0.35 Z_\odot$ ($Z \approx 0.005$). This estimate places SN2019dge's host galaxy in the lowest 10% of the distribution of SNe Ibc host galaxy metallicities

(Sanders et al. 2012), and it is on the lowest 15% in the range of Type Ic-BL SNe host galaxy metallicities (Modjaz et al. 2020)
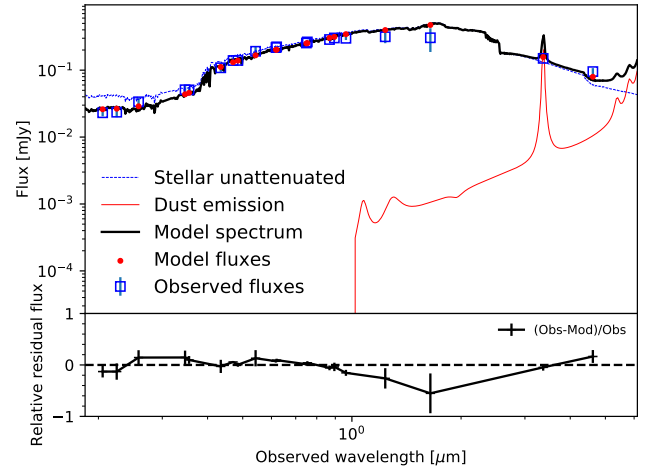

Figure 12. Spectral energy distribution of the host galaxy of SN2019dge. The observed photometric data (with 1σ error bars) are shown in blue open squares, and the model is shown as a black curve ($\chi^2 = 0.64$). The relative residual flux is shown in the bottom panel.

We determine the stellar mass ($M_\star$) of the host galaxy by SED modeling using CIGALE (Boquien et al. 2019). We adopt the stellar population synthesis models from Bruzual & Charlot (2003) with the Kroupa IMF (Kroupa 2001), and assume a double declining exponential star formation history (SFH). In addition, a dust

component is added using the Draine & Li (2007) model to account for dust emission. Finally, the total SED model is attenuated by a modified Calzetti extinction law (Calzetti et al. 2000). It assumes that the young stellar population is extincted by the normal Calzetti law, and the old stellar population is extincted less heavily than that by a certain factor (< 1, Charlot & Fall 2000).

The fitted SED is shown in Figure 12. The derived total stellar mass is $\log(M_{\star,\mathrm{tot}}/M_\odot) = 8.5 \pm 0.1$, the mass of the stars alive is $\log(M_{\star,\mathrm{alive}}/M_\odot) = 8.4 \pm 0.1$, and the inferred SFR is $0.030 \pm 0.005\ M_\odot\,\mathrm{yr}^{-1}$, comparable to the measurement inferred from Hα. The host extinction, $E(B-V)$, is $0.07 \pm 0.02\,\mathrm{mag}$ and $0.03 \pm 0.01\,\mathrm{mag}$ for the young and old stellar population, respectively, both of which are insignificant. The stellar mass and the SFR of the this galaxy are in the lower half of the hosts of Type Ibc SN in the PTF sample (Schulze et al. in prep.).

4. Modeling

4.1. Shock Cooling Powered Fast Rise

Supernovae light curves are mainly powered by shock energy or radiative diffusion from a heating source. We first examine if the peak of SN2019dge is likely to be powered by the radioactive decay of $^{56}\mathrm{Ni}\rightarrow^{56}\mathrm{Co}\rightarrow^{56}\mathrm{Fe}$. With a peak luminosity of $L_{\mathrm{peak}} \approx 5 \times 10^{42}\,\mathrm{erg\,s}^{-1}$ and a rise time of $t_{\mathrm{peak}} \approx 2$–4 d, SN2019dge falls into the unshaded region of Kasen (2017, their Figure 1), where an unphysical condition of $M_{\mathrm{Ni}} > M_{\mathrm{ej}}$ is required. Therefore, we rule out radioactivity as the power source for the fast rise of the light curve.

There have been clues for the early emission mechanism of SN2019dge,:

  (i) The fast t_{rise} (Figure 3), high initial high temperature (middle panel of Figure 4), blue color (Figure 5), and relatively fast color evolution of SN2019dge are reminiscent of shock cooling emission (Nakar & Piro 2014; Piro 2015).

  (ii) The color jump in $g-r$ is observed 6–9 days after maximum (left panel of Figure 5). It is at roughly this phase that the change in bolometric luminosity decline rate transitions from $0.36\,\mathrm{mag\,d}^{-1}$ to $0.11\,\mathrm{mag\,d}^{-1}$ (upper panel of Figure 4). This supports the idea that the dominant power mechanisms before and after this transition are different.

Therefore, we model the early light curve as cooling emission from shock-heated extended material, which is located at the outer layers of the progenitor or outside of the progenitor. We use models presented by Piro (2015, hereafter P15) to constrain the mass and radius of the
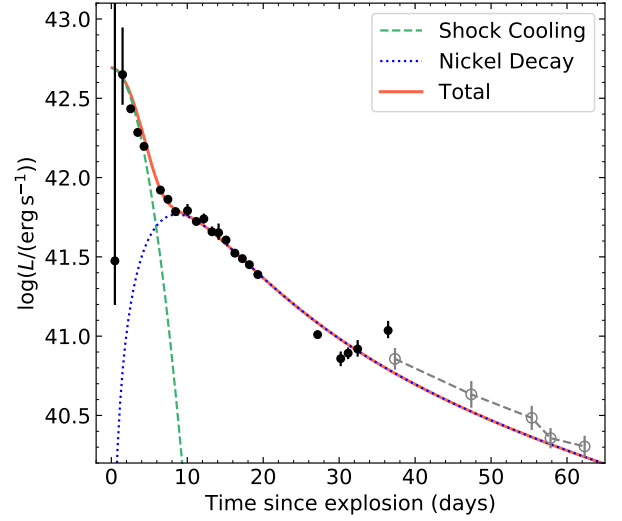

Figure 13. Bolometric light curve for SN2019dge. Latetime quasi-bolometric light curve estimated by computing νL_ν in r-band is shown as empty grey circles. The dashed green and dotted blue lines show the best fits of shock cooling and nickel decay models. The solid red line shows the combination of the two components.

extended material (M_{ext} and R_{ext}, respectively), where M_{ext} includes only mass concentrated around R_{ext}. This model is built on analytical results of Nakar & Piro (2014). Details of the model fitting to multi-band observations are illustrated in Appendix B.2.

In Figure 13, the bolometric light curve measured in Section 3.1 is shown in black. We also show late-time r-band νL_ν measurements in grey empty circles as a proxy of bolometric light curve evolution. The dashed green line shows the best-fit model of $M_{\mathrm{ext}} = 9.34 \pm 0.36 \times 10^{-2} M_\odot$, $R_{\mathrm{ext}} = 2.71^{+0.19}_{-0.17} \times 10^{12}\,\mathrm{cm}$ (i.e., $39.0^{+2.7}_{-2.5} R_\odot$), and explosion epoch at phase $t_{\mathrm{exp}} = -3.21 \pm 0.04\,\mathrm{d}$ (i.e., the explosion occurred 0.45 d before the first detection in g-band). The amount of energy passed into the extended material is well constrained to be $E_{\mathrm{ext}} = (1.15 \pm 0.07) \times 10^{50}\,\mathrm{erg}$.

Given the simple assumptions of the model, we expect the constraints on M_{ext} and R_{ext} to be only approximately accurate. We thus conclude that the early shock cooling emission was produced by an extended envelope with a mass of $\sim 0.1\,M_\odot$ locating at a radius of $\sim 3 \times 10^{12}\,\mathrm{cm}$ ($40\,R_\odot$). There are now numerous cases of early cooling envelope emission observed in CCSNe, where the extended material is estimated to have lower mass (~ 0.001–$0.01\,M_\odot$) and larger radius ($\sim 10^{13}\,\mathrm{cm}$) compared to SN2019dge (Modjaz et al. 2019).

4.2. Mass-Loss Estimate from He II

Early-time low-velocity He II $\lambda 4686$ emission (Section 3.2.1) has been detected in nearly twenty hydrogen-rich CCSNe and one hydrogen-poor SN iPTF14gqr. This feature often fades away within a few hours to a few days after the explosion (Yaron et al. 2017). The high ionization potential of this line requires high temperature or an ionizing flux, which might come from either shock breakout or CSM interaction (Gal-Yam et al. 2014; Smith et al. 2015). Due to the rapid decrease in T_{bb} at the three epochs of our early-time spectra and the similarity between SN2019dge and iPTF14gqr, we favor shock cooling emission as the origin of recombination helium lines. Therefore, we can use the luminosity of the He II $\lambda 4686$ line to make an order-of-magnitude estimate on properties of the emission material, following the procedure given by Ofek et al. (2013a) and De et al. (2018b).

Assuming that the immediate CSM around the progenitor has a spherical wind-density profile of the form $\rho = Kr^{-2}$, where r is distance from the progenitor, $K \equiv \dot{M}/(4\pi v_{w})$ is the wind density parameter, v_{w} is the wind velocity, and $\dot{M}$ is the mass-loss rate. The integrated mass of the emitting material from r to r_1 is

$$M_{\mathrm{He}} = \int_r^{r_1} 4\pi r^2 \rho(r)\mathrm{d}r = 4\pi K \beta r \qquad (1)$$

where $\beta \equiv (r_1 - r)/r$ is assumed to be of order unity.

We can relate the mass of the He II region to the He II $\lambda 4686$ line luminosity using

$$L_{\lambda 4686} \approx \frac{A n_e M_{\mathrm{He}}}{m_{\mathrm{He}}}. \qquad (2)$$

Here

$$A = \frac{4\pi j_{\lambda 4686}}{n_e n_{\mathrm{He}^{++}}}, \qquad (3)$$

$j_{\lambda 4868}$ (in $\mathrm{erg\,cm^{-3}\,s^{-1}\,sr^{-1}}$) is the emission coefficient for the $\lambda 4686$ transition. m_{He} is mass of a helium nucleus, $n_{\mathrm{He}^{++}}$ is the number density of doubly ionized helium and n_e is the number density of electrons.

Assuming a temperature of 10^4 K, electron density of $10^{10}\,\mathrm{cm^{-3}}$, and Case B recombination, we get $A = 1.32 \times 10^{-24}\,\mathrm{erg\,cm^3\,s^{-1}}$ (Storey & Hummer 1995). Using $n_e = 2 n_{\mathrm{He}^{++}}$ and the density profile, Eq. (2) can be written as

$$L_{\lambda 4686} \approx \frac{8\pi A \beta}{m_{\mathrm{He}}^2} \frac{K^2}{r}. \qquad (4)$$

The location of the emitting region can be constrained by requiring that the Thompson optical depth (τ) in the region must be small for the lines to escape. We require

$$\tau = n_e \sigma_{\mathrm{T}} \int_r^{r_1} \mathrm{d}r = \frac{2\sigma_{\mathrm{T}} K \beta}{m_{\mathrm{He}} r} \lesssim 1 \qquad (5)$$

Thus

$$r^2 \gtrsim \left(\frac{2\sigma_{\mathrm{T}}\beta}{m_{\mathrm{He}}}\right)^2 \frac{L_{\lambda 4686} m_{\mathrm{He}}^2 r}{8\pi A \beta} \qquad (6a)$$

$$r \gtrsim L_{\lambda 4686} \frac{\sigma_{\mathrm{T}}^2 \beta}{2\pi A} \qquad (6b)$$

The $+0.4$ d emission line flux is measured to be $F = (8.99 \pm 0.71) \times 10^{-16}\,\mathrm{erg\,cm^{-2}\,s^{-1}}$, corresponding to $L_{\lambda 4686} = 9.0 \times 10^{38}\,\mathrm{erg\,s^{-1}}$. Hence, we get $r \gtrsim 4.8 \times 10^{13}\beta\,\mathrm{cm}$, $K \gtrsim 1.2 \times 10^{14}\,\mathrm{g\,cm^{-1}}$, and $M_{\mathrm{He}} \gtrsim 3.7 \times 10^{-5}\beta^2\,M_\odot$. Adopting a wind velocity of $v_{w} \approx 550\,\mathrm{km\,s^{-1}}$ as measured from the He II FWHM, the mass-loss rate can be constrained to be $\dot{M} \gtrsim 1.1 \times 10^{-4}\,M_\odot\,\mathrm{yr^{-1}}$. Note that these estimates can be affected if the CSM cannot be well characterized by a spherically symmetric $\rho(r) \propto r^{-2}$ density profile, or if the emitting region was confined to a thin shell ($\beta \ll 1$).

4.3. Constraints from Radio Upper Limits

Radio emission in SNe is produced by shock accelerated electrons in the circumstellar material as they gyrate in the post-shock magnetic field when the shock freely expands. Should the circumstellar medium be formed by a pre-SN stellar wind, the radio synchrotron radiation can be used to probe the pre-explosion mass-loss (Chevalier 1982). High frequency ($\nu > 90\,\mathrm{GHz}$) bright ($\nu L_\nu \gtrsim 10^{40}\,\mathrm{erg\,s^{-1}}$) radio sources are often found to be associated with gamma-ray bursts (GRBs), TDEs, and relativistic transients (see Figure 6 of Ho et al. 2019a). Among normal SNe Ibc, moderate submillimeter luminosity at $\sim 5 \times 10^{37}\,\mathrm{erg\,s^{-1}}$ has been observed in SN1993J (Weiler et al. 2007) and SN2011dh (Horesh et al. 2013).

Our SMA observations constrain the submillimeter luminosity of SN2019dge to $\nu L_{\nu,230\mathrm{GHz}} < 5.3 \times 10^{39}\,\mathrm{erg\,s^{-1}}$ and $\nu L_{\nu,345\mathrm{GHz}} < 3.0 \times 10^{40}\,\mathrm{erg\,s^{-1}}$. We place these upper limits in physical context using the synchrotron self-absorption model given by Chevalier (1998). The expected radio luminosities are computed at 230 and 345 GHz for two types of circumstellar environments — one with a wind-density with the same parameterization as that adopted in Section 4.2 and the other with a constant-density environment ($\rho = $ constant).

Adopting the explosion epoch found in Section 4.1, our SMA observations were obtained at 2.75 day after explosion. Given the early time of these observations, we consider constant shock velocities at 0.1–0.25c, as found to be typical in SNe Ibc (Wellons et al. 2012). We assume an electron energy power-law index of $p = 3$, a volume filling factor $f = 0.5$, and that the electrons and magnetic field in the post-shock region share constant
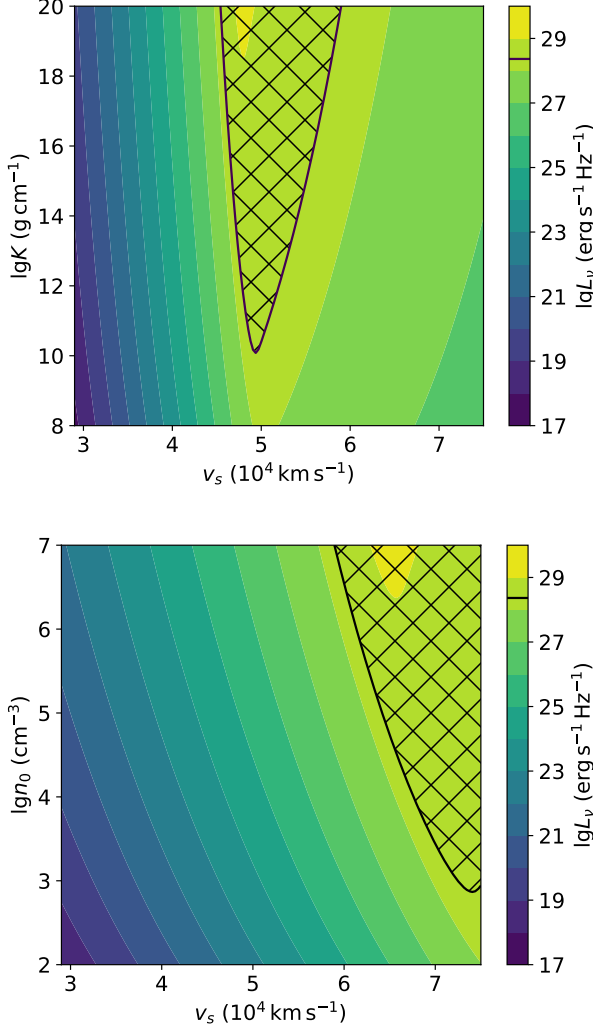
Figure 14. Maps of expected radio luminosity at 230 GHz. The x-axis is the shock velocity v_s. The y-axis is wind mass-loss parameter K in the case of $\rho \propto r^{-2}$ CSM environment in the upper panel, while in the bottom panel it is the number density n_0 in the constant-density case. The black contour in each panel shows the location of 3σ upper limit at 230 GHz on SN2019dge. The phase space with a luminosity higher the black line in each panel is ruled out by the observation.

fractions of the post-shock energy density, i.e., $\epsilon_e = \epsilon_B = 0.1$.

The expected radio luminosity predicted by the Chevalier model in the two environments at 230 MHz are shown in Figure 14 by the color maps, and the black contours indicate our 3σ limits. As can be seen, only small regions have expected luminosity higher than the 3σ limits (indicated by the hatched regions), and thus our observations are not deep enough to provide stringent constrains on the circumstellar properties. Com-

pared with 230 MHz, the parameter space is even more poorly constrained at 350 GHz and are thus not shown.

4.4. Radioactivity Powered Main Peak

After subtracting the shock cooling emission from the bolometric light curve, the remaining light curve has a peak luminosity of $L_{\rm peak} \approx 6 \times 10^{41}\,{\rm erg\,s^{-1}}$ and a rise time of $t_{\rm peak} \approx 9\,{\rm d}$. In the shaded region of Kasen (2017, Fig. 1), this falls between the $M_{\rm Ni} = 0.1\,M_{\rm ej}$ and $M_{\rm Ni} = 0.01\,M_{\rm ej}$ lines, indicating that the remaining component can be powered by ^{56}Ni decay. Apart from this, the moderate $t_{\rm decay}$ of SN2019dge (bottom panel in Figure 3) is similar to that found in a few Ca-rich transients, and consistent with coming from radioactivity. Here we use two methods to estimate $M_{\rm ej}$ and $M_{\rm Ni}$.

First of all, we use analytical models (Arnett 1982; Valenti et al. 2008; Wheeler et al. 2015) to constrain the nickel mass ($M_{\rm Ni}$), a characteristic photon diffusion timescale ($\tau_{\rm m}$), and a characteristic γ-ray escape timescale (t_0). Details of the model fitting are given in Appendix B.3. The dotted blue line in Figure 13 shows the best-fit model of $M_{\rm Ni} = 1.61^{+0.04}_{-0.03} \times 10^{-2} M_\odot$, $\tau_{\rm m} = 6.35 \pm 0.18\,{\rm d}$, and $t_0 = 24.04^{+0.76}_{-0.73}\,{\rm d}$. Thus, using Equation (B9), the ejecta mass can be estimated to be

$$M_{\rm ej} = 0.36 \pm 0.02 \left(\frac{v_{\rm ej}}{8000\,{\rm km\,s^{-1}}} \right) \left(\frac{0.07\,{\rm cm^2\,g^{-1}}}{\kappa_{\rm opt}} \right) M_\odot \tag{7}$$

Here we adopt the the mean opacity of SNe Ibc found by Taddia et al. (2018). In Section 3.2.2, the the photospheric velocity of $\approx 6000\,{\rm km\,s^{-1}}$ is measured at phase $\Delta t \sim 12\,{\rm d}$ (i.e., ~ 15–16 d post explosion). At that time, Figure 4 shows that $R_{\rm bb}$ stays roughly flat, indicating that a certain amount of ejecta in the outer layers should have a velocity greater than that measured from the He I absorption minimum. Therefore, we adopt the $\approx 8000\,{\rm km\,s^{-1}}$ measured from early $R_{\rm bb}$ evolution (see Section 3.1.2) to be a more appropriate estimate for $v_{\rm ej}$. The kinetic energy is then calculated to be

$$E_{\rm kin} = \frac{3}{10} M_{\rm ej} v_{\rm ej}^2 = (1.36 \pm 0.08) \times 10^{50}\,{\rm erg} \tag{8}$$

Khatami & Kasen (2019, hereafter KK19) presented improved analytic relations (compared with the original Arnett 1982 model) between $t_{\rm peak}$ and $L_{\rm peak}$. When $t < 10\,{\rm d}$, $\varepsilon_{\rm Ni}(t) \gg \varepsilon_{\rm Co}(t)$ (see Equations B5, B6), and hence we have an exponential heating function

$$L_{\rm heat}(t) = L_0 e^{-t/\tau_{\rm Ni}} \tag{9}$$

where $L_0 = M_{\mathrm{Ni}} \times \epsilon_{\mathrm{Ni}}$. In this case, KK19 (Eq. 21) shows that the relation between peak time and luminosity is:

$$L_{\mathrm{peak}} = \frac{2L_0 \tau_{\mathrm{Ni}}^2}{\beta^2 t_{\mathrm{peak}}^2} \left[1 - (1 + \beta t_{\mathrm{peak}}/\tau_{\mathrm{Ni}}) e^{-\beta t_{\mathrm{peak}}/\tau_{\mathrm{Ni}}} \right] \quad (10)$$

where $\beta \sim 4/3$ gives a reasonable match to numerical simulations. With $L_{\mathrm{peak}} \approx 6 \times 10^{41} \,\mathrm{erg\,s^{-1}}$ and $t_{\mathrm{peak}} \approx 9\,\mathrm{d}$, we get an estimate of $M_{\mathrm{Ni}} \sim 0.017\,M_\odot$.

M_{ej} can be estimated using Eq. 23 of KK19:

$$\frac{t_{\mathrm{peak}}}{t_{\mathrm{d}}} = 0.11 \ln \left(1 + \frac{9\tau_{\mathrm{Ni}}}{t_{\mathrm{d}}} \right) + 0.36, \quad (11)$$

where t_{d} is the characteristic timescale without any numerical factors

$$t_{\mathrm{d}} = \left(\frac{\kappa_{\mathrm{opt}} M_{\mathrm{ej}}}{v_{\mathrm{ej}} c} \right)^{1/2}. \quad (12)$$

We derive $t_{\mathrm{d}} \approx 15.4\,\mathrm{d}$, which implies

$$M_{\mathrm{ej}} \approx 0.30 \left(\frac{v_{\mathrm{ej}}}{8000\,\mathrm{km\,s^{-1}}} \right) \left(\frac{0.07\,\mathrm{cm^2\,g^{-1}}}{\kappa_{\mathrm{opt}}} \right) M_\odot \quad (13)$$

The kinetic energy of the ejecta is then $E_{\mathrm{kin}} \approx 1.2 \times 10^{50}\,\mathrm{erg}$.

In conclusion, the estimates derived from simplified model fitting and new analytic relations from KK19 are roughly the same. Ejecta mass ($M_{\mathrm{ej}} \sim 0.3 M_\odot$), nickel mass ($M_{\mathrm{Ni}} \sim 0.017 M_\odot$), and total kinetic energy ($E_{\mathrm{kin}} \sim 1.2 \times 10^{50}\,\mathrm{erg}$) from the explosion of SN2019dge are very small.

5. Interpretation

5.1. A Core-Collapse Supernova

At early times, the cooling emission from shock-heated surrounding material of $M_{\mathrm{ext}} \sim 0.1\,M_\odot$ and $R_{\mathrm{ext}} \sim 3 \times 10^{12}\,\mathrm{cm}$ ($40\,R_\odot$) corroborates that the progenitor of SN2019dge is a star with an extended envelope. Indeed stellar evolution models predict envelope radii of 10–$100\,R_\odot$ for helium stars with zero-age helium core masses within 2.5–$3.2\,M_\odot$ that have stripped all of the hydrogen-rich envelope (Woosley 2019; Laplace et al. 2020). Therefore, the early-time shock cooling light curve serves as strong evidence that SN2019dge is the explosion of a star with inflated radius (not a compact object).

The ^{56}Ni mass of $\sim 0.017\,M_\odot$ inferred from the radioactivity-powered decay is much greater than that produced in electron-capture SNe ($\sim 10^{-3}\,M_\odot$, Moriya et al. 2014), whereas the ejecta velocity of $v_{\mathrm{ej}} \approx 6000\,\mathrm{km\,s^{-1}}$ is larger than that expected in fallback SNe ($\sim 3000\,\mathrm{km\,s^{-1}}$, Moriya et al. 2010). Therefore, we conclude that SN2019dge is associated with the class of iron CCSNe.

5.2. An Ultra-Stripped Progenitor

As noted in the introduction, the majority of SNe Ibc, with M_{ej} in the range of 1–5 $M_\odot$, are believed to come from binary evolution. The small amount of ejecta mass seen in SN2019dge ($M_{\mathrm{ej}} \sim 0.3\,M_\odot$) requires extreme stripping prior to the explosion in a binary system, which suggests an ultra-stripped progenitor (Tauris et al. 2013).

Compared with iPTF14gqr, where the second peak of the light curve suggests $M_{\mathrm{ej}} \sim 0.2\,M_\odot$, SN2019dge has a higher ejecta mass. In particular, the helium-rich photospheric spectra indicate that SN2019dge has a greater amount of helium in the ejecta. He I emission lines are non-thermally excited by collisions with fast electrons, which result from Compton processes with γ-rays from ^{56}Ni decay (Dessart et al. 2012; Hachinger et al. 2012). On the other hand, the weak absorption strength in the He I P-Cygni profile (Figure 7 and Figure 8) suggests that the helium envelope mass of SN2019dge is substantially lower than that in a canonical Type Ib SN (Fremling et al. 2018). The stripping in SN2019dge is therefore less extreme than for iPTF14gqr. Nevertheless, the striking similarities between these two events indicate that they probably originate from similar channels.

The He II $\lambda 4686$ flash ionized emission comes from optically thin material located at $\sim 5 \times 10^{13}\,\mathrm{cm}$ ($700\,R_\odot$). This is even larger than the expected orbital separation required for extreme stripping. Therefore, material at such a large radius might be ejected prior to the explosion, where the mass-loss timescale is roughly a few days[5]. The inferred mass-loss rate of $\dot{M} \gtrsim 10^{-4}\,M_\odot\,\mathrm{yr}^{-1}$ is much higher than that observed in Galactic Wolf-Rayet stars (Smith 2014). The photospheric and late-time spectra of SN2019dge signify interaction with a helium-rich extended dense shell, which may also consist of gas originally ejected by the progenitor as a stellar wind or deposited by binary interaction. The high mass-loss rate and short ejection timescale can be achieved in the final stages of stellar evolution by several mechanisms: 1) a powerful outflow driven by super-Eddington wave energy deposition during the last few years before explosion (Quataert & Shiode 2012), 2) explosive mass ejection due to violent silicon flashes within a few weeks before the explosion of low-mass helium stars (Woosley 2019), 3) nonconservative mass transfer in binary evolution of ultra-stripped stars (Tauris et al. 2015).

5.3. Stellar Evolution Pathways

---

[5] Estimated by $\sim 700\,R_\odot / 550\,\mathrm{km\,s^{-1}}$

Table 3. Model parameters for hydrogen-poor subluminous fast-evolving SNe where the bolometric light curve can be fitted with a shock cooling powered component and a radioactivity powered component.

Name	$v_{\rm ej}$	$\tau_{\rm m,A82}$	$M_{\rm ej,A82}$	$M_{\rm Ni,A82}$	$M_{\rm ej,KK19}$	$M_{\rm Ni,KK19}$	$R_{\rm ext}$	$M_{\rm ext}$
	$({\rm km\,s^{-1}})$	(d)	$(M_\odot)$	$(10^{-2}M_\odot)$	$(M_\odot)$	$(10^{-2}M_\odot)$	$(10^{12}\,{\rm cm})$	$(10^{-2}M_\odot)$
iPTF14gqr	10000	$4.38^{+0.14}_{-0.15}$	$0.21^{+0.01}_{-0.01}$	$8.01^{+0.14}_{-0.15}$	0.22	8.35	$55.33^{+9.73}_{-9.68}$	$1.46^{+0.37}_{-0.27}$
iPTF16hgs	10000	$11.09^{+1.08}_{-1.09}$	$1.36^{+0.28}_{-0.25}$	$2.33^{+0.23}_{-0.23}$	0.78	2.29	$1.67^{+2.24}_{-0.95}$	$8.94^{+3.77}_{-2.61}$
SN2018lqo	8250	$9.71^{+0.52}_{-0.37}$	$0.86^{+0.09}_{-0.06}$	$2.75^{+0.09}_{-0.07}$	0.63	3.08	$26.80^{+108.58}_{-23.55}$	$4.82^{+3.23}_{-1.15}$
SN2019dge	8000	$6.35^{+0.18}_{-0.18}$	$0.36^{+0.02}_{-0.02}$	$1.61^{+0.04}_{-0.03}$	0.30	1.70	$2.71^{+0.19}_{-0.17}$	$9.34^{+0.36}_{-0.36}$

NOTE—Model parameters with the subscripts of "A82" and "KK19" refers to radioactivity-powered ligth curve models of Arnett (1982) (see Appendix B.3) and Khatami & Kasen (2019), respectively. Reference: iPTF14gqr (De et al. 2018b), iPTF16hgs (De et al. 2018a), SN2018lqo (De et al. 2020a), SN2019dge this work.

Here we discuss possible evolution paths of SN2019dge's progenitor.

We first consider the scenario where SN2019dge comes from a binary consisting of two massive stars. Yoon et al. (2010) show that stripping is very inefficient at subsolar metallicity of $Z \approx 0.004$ (similar to the $Z \approx 0.005$ calculated in Section 3.3), such that the final mass of the primary at the time of core-collapse will be higher than $3.8\,M_\odot$. This will lead to $M_{\rm ej} \gtrsim 2.3\,M_\odot$ assuming that the explosion forms a neutron star of $1.5\,M_\odot$. The inferred ejecta mass is much higher than the observed ($M_{\rm ej} \sim 0.3\,M_\odot$). We thus conclude that this scenario is not consistent with observations of SN2019dge. to-do: say that you cannot have two massive stars to do this. this paragraph is relevant

We next consider the possibility that the companion is a lower mass ($< 10\,M_\odot$) main sequence star. Zapartas et al. (2017) performed population synthesis simulations, showing that for the pre-SN helium star to reach $< 2\,M_\odot$, a relatively high initial mass ratio is needed. Based on this result, De et al. (2018b) disfavored this scenario for the progenitor of iPTF14gqr, since a small mass ratio is required to enable a narrow orbit where the helium star undergoes mass-loss via Roche-lobe overflow (RLO) to achieve extreme stripping. Their argument also applies here.

Finally, we consider scenarios where the progenitor resides in a tight helium star + degenerate object system, where the degenerate object can be a white dwarf, a neutron star, or a black hole. This scenario is supported by the high efficiency of mass transfer to compact companions via Case BB/BC RLO in the production of almost bare CO cores with little helium envelope (Dewi et al. 2002; Tauris et al. 2012).

The final mass of the helium envelope depends on the initial mass of the helium star and the orbital period of the compact binary. To reconcile with the ejecta mass observed in SN2019dge, one may expect small final envelope mass ($\lesssim 0.3\,M_\odot$) but large enough for optical helium features to be observed in the SN explosion ($\gtrsim 0.06\,M_\odot$, Hachinger et al. 2012). This can be achieved in a system where the progenitor is a helium star in a compact binary with $0.1 \lesssim P_{\rm orb} \lesssim 20$ d (Tauris et al. 2015). Therefore, we conclude that the observational characteristics of SN2019dge can be best explained by a compact companion.

The outcome of SN2019dge — an iron core-collapse ultra-stripped SN — is a neutron star with mass in the range 1.1–$1.8\,M_\odot$ (Tauris et al. 2015). The small ejecta mass and the small binding energy of the stripped envelope imply a small kick velocity ($\sim 50\,{\rm km\,s^{-1}}$) imparted onto the newborn NS (Tauris et al. 2015; Suwa et al. 2015; Bray & Eldridge 2016; Müller et al. 2018), which can prevent the binary system from being disrupted or broken up, leaving a compact NS binary (Tauris et al. 2017). Ultra-stripped iron CCSNe therefore serve as a natural formation channel for compact NS binaries with small eccentricities.

5.4. Comparison with Other Ultra-Stripped SN Candidates

In addition to SN2019dge and iPTF14gqr, we search the literature for other subluminous fast-evolving hydrogen-poor SNe whose light curves can potentially be well fitted by an early-time shock-cooling component from an extended envelope and a radioactivity-powered second peak with small $M_{\rm ej}$. We recover iPTFF16hgs (De et al. 2018a) and SN2018lqo (De et al. 2020a) as ultra-stripped SN candidates. Here we apply our modeling approach described in Section 4.1 and 4.4 to iPTF16hgs and SN2018lqo to distill the physical parameters of these two events. We show the results in Table 3. The ejecta masses of iPTF16hgs and SN2018lqo are greater than that in SN2019dge and iPTF14gqr by a

factor of ~ 3, and falls inside the range of M_{ej} expected in explosions of a helium star orbiting a compact object, but is at the upper side of the boundaries (Tauris et al. 2015). However, SN2018lqo occurs in an elliptical galaxy, which is not expected to be the host for ultra-stripped SNe.

A full discussion of the progenitors of iPTF16hgs and SN2018lqo is beyond the scope of this paper. Here we refer to a recent study conducted by De et al. (2020a), which classify these two objects into the "green Ca-Ib" subclass in the Ca-rich SNe category. This class of objects is spectroscopically similar to SNe Ib at maximum light, and do not exhibit line-blanketed continua at ~ 3500–5500 Å. De et al. (2020a) proposed that pure helium-shell detonations or deflagrations can explain their photometric and spectroscopic properties. In this scenario, the early-time peak might be caused by radioactive decay from short-lived isotopes in the outermost ejecta, and the main peak is powered by ^{56}Ni decay.

Although we only include hydrogen-poor events in this comparison, we note that SN2019ehk, which exhibit flash ionized hydrogen in its early-time spectra (Jacobson-Galán et al. 2020), is also suggested to be an ultra-stripped CCSN (Nakaoka et al. 2020).

6. Rates

As progenitors of compact neutron star binaries, the volumetric rates of ultra-stripped SNe have implications for our understanding of the evolutionary pathways leading to these systems and the gravitational waves detected by existing and upcoming facilities such as LIGO/VIRGO (Abbott et al. 2017a).

Based on population synthesis calculation, Tauris et al. (2015) estimate that the volumetric rates of ultra-stripped SNe should be ~ 0.1–1% of the rate of Core-collapse SNe. Using the properties of the promising ultra-stripped SN iPTF14gqr (De et al. 2018b), Hijikawa et al. (2019) estimate the volumetric rates of iPTF14gqr-like ultra-stripped SNe to be $\sim 2 \times 10^{-7}\,\mathrm{Mpc}^{-3}\,\mathrm{yr}^{-1}$, or $\sim 0.2\%$ of the local CCSNe rate (Li et al. 2011a). However, since existing ultra-stripped SN candidates were found outside of systematic SN classification efforts, observationally constraining the rates of ultra-stripped SNe has not been possible thus far.

6.1. Simple Estimation

6.1.1. Using the BTS Sample

SN2019dge was followed up as a part of the ZTF Bright Transient Survey (BTS, Fremling et al. 2019b) that aims to spectroscopically classify all extragalactic transients in ZTF brighter than 18.5–19 mag at peak.

Since BTS only reads from the ZTF public alert stream (highlighted with a greater marker size in Figure 15), SN2019dge peaks between 18.5 and 19.0 mag in the BTS sample. Thanks to the relatively high spectroscopic completeness ($\approx 89\%$) at the brightness limit of 19.0 mag, we can directly place constraints on the rates of 19dge-like ultra-stripped SNe using the BTS sample.
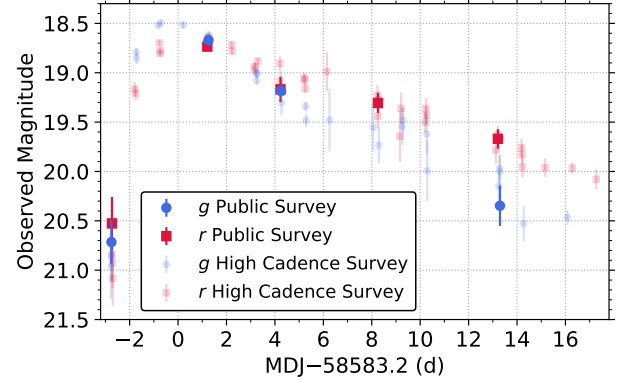

Figure 15. Un-binned P48 light curve of SN2019dge. We highlight observations obtained in the public Northern Sky Survey in a greater marker size and high-opacity colors, while observations obtained in the high-cadence survey are shown in semi-transparent.

SN2019dge peaked at an absolute magnitude of -16.44 mag in g-band. At the BTS peak brightness limit of 19.0 mag, objects similar to SN2019dge would be detectable out to 123 Mpc. Thus, taking only the local 123 Mpc volume within redshift of $z = 0.028$, we compare the number of CCSNe brighter than 19.0 mag at peak that were found in the BTS experiment in its first 12 months of operations (between 2018-06-01 and 2019-06-01). In this time period, BTS classified a total of 116 CCSNe in this volume. As such, the detection of one object in this sample constrains the rate of ultra-stripped SNe to be $\sim 0.86\%$ of the CCSNe rate brighter than $M = -16.44$ mag in this volume.

Taking the observed luminosity function of CCSNe in the local universe (Li et al. 2011b), we find that $\approx 50\%$ of CCSNe are fainter than $M = -16.44$ mag. The luminosity function corrected rate of 19dge-like events is then $\sim 0.43\%$ of the local CCSNe rate. The inferred rate is consistent with that estimated in Tauris et al. (2015), but higher than that inferred for iPTF14gqr-like events (Hijikawa et al. 2019). Adopting the CCSNe volumetric rate of $0.7 \times 10^{-4}\,\mathrm{Mpc}^{-3}\,\mathrm{yr}^{-1}$ (Li et al. 2011a), the volumetric rate of 19dge-like ultra-stripped SNe rate is $\sim 300\,\mathrm{Gpc}^{-3}\,\mathrm{yr}^{-1}$. This rate estimation is only a lower limit, since the fast photometric evolution of objects

similar to SN2019dge can be easily missed due to the slower 3-day cadence of the ZTF public survey.

6.1.2. Using the CLU sample

The ZTF team also conducts a campaign to spectroscopically classify all SNe within 200 Mpc by filtering transients occurring in galaxies with previously known redshifts within $z \leq 0.05$ in the Census of the Local Universe (CLU) catalog (De et al. 2020a). Hereafter we refer this experiment as CLU. The spectroscopic completeness of transients in the CLU sample that had at least one detection brighter than 20 mag is 89%. Since CLU reads from the whole ZTF alert stream (e.g., all data points shown in Figure 15), the higher-cadence subsurveys allow it to better characterize fast-evolving SNe. However, the uncertainty in this experiment is the incompleteness of the input galaxy catalog. The redshift completeness factor (RCF) is $\approx 80\%$ at the lowest redshifts and decreases to $\approx 50\%$ at $z = 0.05$, as measured by the BTS experiment (Fremling et al. 2019b).

At the CLU peak brightness limit of 20.0 mag, objects similar to SN2019dge would be detectable out to 195 Mpc. Between 2018-06-01 and 2019-06-01, CLU classified a total of 273 CCSNe in this volume, whereas no good ultra-stripped SN candidates have been identified. This might be used to place an upper limit of ultra-stripped SNe rate following the simple calculation described in Section 6.1.1 to-do: 1/273 * (7e-4 * 1e+9). However, it is also susceptible to the fast evolution of 19dge-like SNe being missed by the observation gaps. In Section 6.2 we attempt to place robust estimates of 19dge-like ultra-stripped SNe rate by running simulated surveys with the ZTF cadence.

6.2. Estimation Based on Survey Simulations

We utilize `simsurvey` (Feindt et al. 2019), a `python` package designed for assessing the rates of transient discovery in surveys like ZTF. To simulate the expected yield of a specific type of transient given a volumetric rate, `simsurvey` requires three inputs: 1) A survey schedule. We use the actual ZTF observing history in g- and r-band between 2018-06-01 and 2019-06-01 in any of the public or collaboration surveys as the input survey plan. 2) A transient model. We construct a light curve template of SN2019dge (see details in Appendix B.4). Using the template, we generate a `TimeSeriesSouce` model in the `sncosmo` package (Barbary et al. 2016). 3) A function to sample the transient model parameters. Transients are injected out to a redshift of $z = 0.044$, since objects further out are not expected to peak brighter than 20.0 mag.

We examine the expected number of detected 19dge-like SNe for a range of input rates. For each input rate, we performed 300 simulations of the ZTF observing plan. In order to select transient candidates that would have passed the selection criteria of the BTS or CLU experiment and been flagged as an object with photometric properties consistent with being a 19dge-like ultra-stripped SN, we apply cuts on the simulated light curves as described below.

For the BTS filter, we only use public survey pointings, and reject SNe at low Galactic latitudes ($|b| \leq 7°$) to be consistent with the BTS experiment (Fremling et al. 2019b). In either the g- or r-band light curve, we identify peak light as the brightest detection in the simulated light curve, and require:

(i) peak magnitude < 19.0 mag

(ii) within 4.1 d before peak, there must be at least one detection or one upper limit deeper than 1.5 mag below peak

(iii) within 15 d after peak, there must be at least three detections, and the measured decline rate must be greater than $0.07 \, \mathrm{mag \, d^{-1}}$.

Criterion (ii) is set to require that the fast rise of the light curve can be recognized from the observation. This is essential since if we only discover SN2019dge at the radioactive tail, we will probably classify it as a low-velocity SN Ib. Criterion (iii) is made to ensure that the rapid decline of the light curve can be captured, such that the small ejecta mass can be inferred.

For the CLU filter, we use all ZTF pointings, and require that in either the g- or r-band light curve:

(i) peak magnitude < 20.0 mag

(ii) the light curve must satisfy at least one of the following criteria: 1) within 4.1 d before peak, there must be at least one detection or one upper limit deeper than 1.5 mag below peak, 2) within 2.5 d before peak, there must be at least one detection deeper than 0.75 mag below peak

(iii) same as criterion (iii) applied in the BTS filter.

We apply the above criteria to the actual observations of CCSNe in the BTS and CLU sample. We identify one other SN — ZTF18abwkrbl (SN2018gjx) — that pass our criteria. However, ZTF18abwkrbl is a SN IIb that clearly shows hydrogen in the spectra, and can therefore be excluded as an ultra-stripped SN candidate (Tauris et al. 2015).

In Figure 16, we show the number of transients that pass our selection criteria as a function of the input volumetric rate. The solid line and shaded region indicate
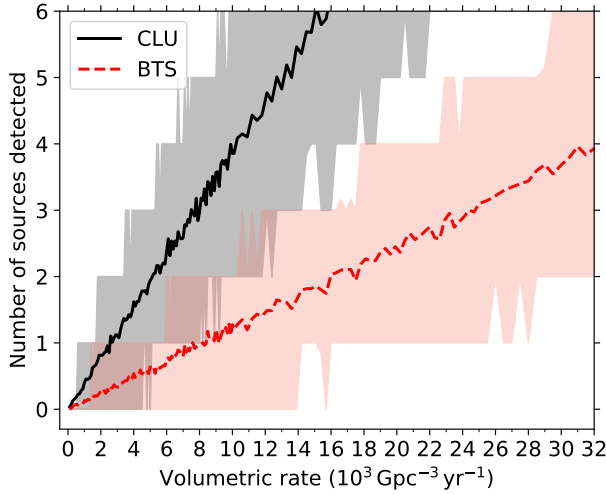
Figure 16. The number of sources passing criteria (described in text) as a function of the input volumetric rate, in both the BTS and CLU experiments. The lines show the mean of the 300 simulations, and the shaded boundaries indicate the 16th and 84th percentiles.

the mean and 68% credible region of the 300 simulations. In the actual BTS experiment, there was only *one* detected ultra-stripped SN. Therefore, we consider the range of volumetric rate where *one* falls within the shaded red region as a constraint on the rate of 19dge-like ultra-stripped SNe. This gives R_{19dge} in the range of 1400–25000 $Gpc^{-3} yr^{-1}$.

Using the fact that there were *zero* ultra-stripped SN detected in the actual CLU experiment, the grey shaded region in Figure 16 might suggest $R_{19dge} \lesssim 4500 \, Gpc^{-3} yr^{-1}$. However, this upper limit needs to be corrected for offset distribution and galaxy catalog incompleteness. First of all, as discussed in De et al. (2020a), the CLU experiment is restricted to transients coincident within $100''$ of the host galaxy nuclei. SN2019dge and iPTF14gqr are $0.5''$ and $24''$ from their host galaxies (all within $100''$). Although a large sample of ultra-stripped SNe is needed to examine the host offset distribution of this class of objects, the fact that they arise from massive binary evolution suggest that the correction due to this factor should be small. Secondly, the incompleteness of the input galaxy catalog possibly leads to an underestimation of ultra-stripped SNe rate by a factor of 55–80%, as indicated by the RCF. We adjust for such an incompleteness by increase the upper limit from 4500 to 8200 $Gpc^{-3} yr^{-1}$.

Combining results from the BTS and CLU experiments, we derive a 19dge-like ultra-stripped SNe rate of 1400–8200 $Gpc^{-3} yr^{-1}$, corresponding to 2–12% of CC-SNe rate.

6.3. Effects of Different Envelope Masses and Radii

Given the low mass of ultra-stripped progenitors, we expect to see shock cooling emission from the inflated pre-explosion star, as has been clearly seen in the case of iPTF14gqr and SN2019dge in the fast early-time evolution and blue colors of the optical light curve. As is shown by Nakar & Piro (2014, Fig. 2), rise time of the shock cooling light curve is determined by mass of the extended material M_{ext}, while the peak luminosity is mainly modulated by R_{ext}. We demonstrate this dependence in Figure 17. We simulate shock cooling light curves by varying M_{ext} and R_{ext}, and at the same time setting $E_{ext} = 1.15 \times 10^{50}$ erg (the value found in SN2019dge).

In the upper panel, t_{rise} is defined in the same way as in Section 3.1.1 (rise time from half-max to max). The rising part of the cooling light curve can be captured by a three-day, two-day, and one-day cadence optical survey at $M_{ext} \gtrsim 0.14 \, M_\odot$, $\gtrsim 0.07 \, M_\odot$, and $\gtrsim 0.03 \, M_\odot$, respectively. Transients with $M_{ext} \gtrsim 0.15 \, M_\odot$ will not pass our selection criteria in Section 6.2. In the bottom panel, we show the expected absolute luminosity at peak of the g-band cooling light curve. As is readily shown, for ultra-stripped progenitors with an extended radius $\lesssim 2 \times 10^{12}$ cm, a survey like ZTF is only sensitive to objects in the local universe ($\lesssim 100$–150 Mpc) for the subsequent evolution of the light curve to be well-characterized. Taken together, we conclude that our estimation of the ultra-stripped SNe rate does not include ultra-stripped progenitors with $M_{ext} \gtrsim 0.15 \, M_\odot$ or $R_{ext} \lesssim 2 \times 10^{12}$ cm.

6.4. Other Uncertainties

The above estimation of the ultra-stripped SNe rate should not be directly compared with double neutron star (DNS) local coalescence rate density (R_{DNS}) for several reasons. First of all, if the companion of the pre-explosion helium star is a white dwarf or a black hole, SN2019dge will not be the progenitor of a double neutron star system, and thus the inferred R_{dge} is not connected with R_{DNS}. Secondly, even in the case that the companion is a neutron star, if the forming DNS binary has orbital periods less than ~ 1 d, it cannot merger within the age of the Universe (Tauris et al. 2015). Future theoretical work is needed to establish the relationship between orbital periods of the pre-explosion binary systems and SNe observational properties. Finally, as noted in the introduction, apart from the ultra-stripped progenitors, DNSs can also form via dynamical capture in a globular cluster (East & Pretorius 2012; Andrews & Mandel 2019). As the fraction of DNSs formed from
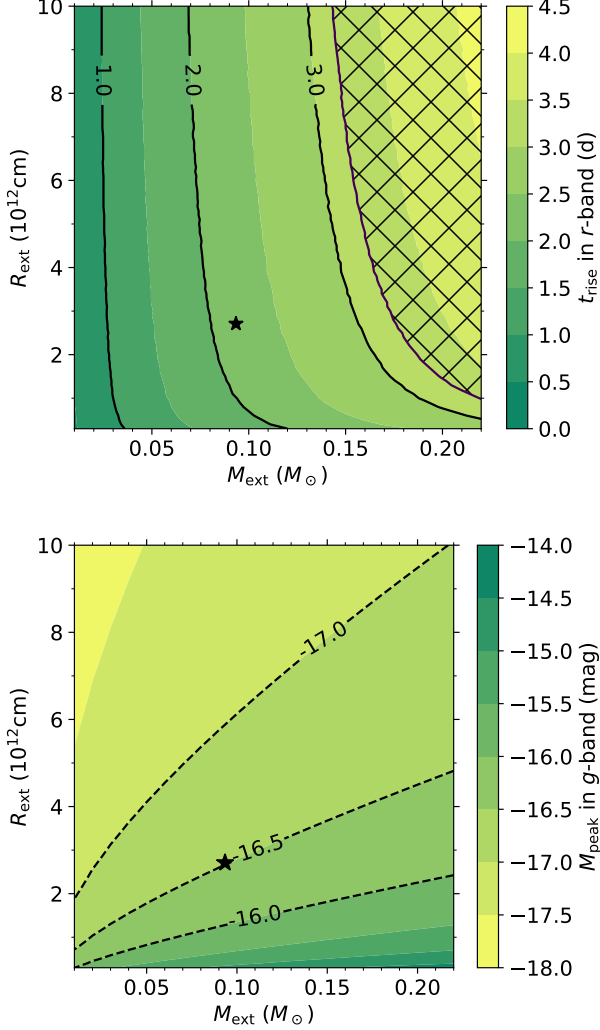
Figure 17. Expected r-band rise time (upper panel) and g-band peak absolute luminosity (bottom panel) as a function of shock cooling model parameters R_{ext} and M_{ext}. The position of SN2019dge is indicated by the black asterisks. In the upper panel, parameter space that could not pass our criteria of "rise from 1.5 mag below peak to peak in less than 4.1 d" (Section 6.2) is indicated by the hatched region.

each channel is not clear, this acts as another uncertainty in relating R_{dge} to R_{DNS}.

7. Conclusion

In this paper we have presented the discovery, observation and modeling of the transient SN2019dge. We summarize the main characteristics of this object below:

(a) Peak absolute magnitudes are $M_{g,peak} \approx -16.5$ mag and $M_{r,peak} \approx -16.3$ mag. In r-band, rise time (half-max to max) is 2.0 d and decay time (max to half-max) is 8.6 d. SN2019dge is one of the most rapidly rising subluminous SNe I discovered to date.

(b) Early-time spectra show a blue continuum and flash He II features that indicate a high mass-loss rate of $\gtrsim 10^{-4} \, M_\odot \, yr^{-1}$.

(c) Photospheric spectra indicate helium-rich ejecta, and the prominent NUV Mg II emission suggests interaction between SN ejecta and CSM.

(d) Late-time spectra show signatures of interaction with helium-rich CSM, similar to that observed in Type Ibn SNe.

(e) SN2019dge exploded only 0.2 kpc away from the nucleus of a compact low-metallicity ($Z \approx 0.005$) galaxy with small star formation rate (SFR $\approx 0.015 \, M_\odot \, yr^{-1}$) and stellar mass ($M_* \approx 2.5 \times 10^8 \, M_\odot$).

(f) The bolometric light curve of SN2019dge peaks at $\sim 5 \times 10^{42} \, erg \, s^{-1}$, and can be explained by a combination of two components. The first component is consistent with shock cooling from an envelope of $\sim 0.1 \, M_\odot$ located at $\sim 3 \times 10^{12} \, cm \, (40 \, R_\odot)$ from the progenitor. The second component is powered by $\sim 0.017 \, M_\odot$ of ^{56}Ni.

(g) We estimate the ejecta mass and kinetic energy of SN2019dge to be 0.25–0.35 $M_\odot$ and 5.5–7.3 $\times 10^{49}$ erg, respectively.

Taken together, we interpret SN2019dge as the first helium-rich ultra-stripped envelope SN.

Based on the one event, we estimate the rate density of 19dge-like ultra-stripped SNe (with $M_{ext} \lesssim 0.15 \, M_\odot$ and $R_{ext} \gtrsim 2 \times 10^{12}$ cm) to be 1400–8200 $Gpc^{-3} \, yr^{-1}$. The first detection of gravitational waves from the merging DNS binary GW170817 gave $R_{DNS} = 320$–4740 $Gpc^{-3} \, yr^{-1}$ (Abbott et al. 2017a). Detection of GW190425 provides an update of $R_{DNS} = 250$–2810 $Gpc^{-3} \, yr^{-1}$ (Abbott et al. 2020). Based on an archival search for EM170817-like transients (known as "kilonovae" or "macronovae") in the PTF database, Kasliwal et al. (2017) reported an upper limit on the rate of 800 $Gpc^{-3} \, yr^{-1}$, which might be doubled if the typical kilonova is 50% fainter than EM170817. Our constraint of R_{19dge} is thus greater than R_{DNS} implied by the LIGO/VIRGO experiment and the upper limit of kilonovae rate estimated from PTF. This can be understood since not all ultra-stripped systems will give NS+NS events (some will give NS+WD, some will give NS+BH, and some may not be compact enough to merge in less than the Hubble time).

It is important to compare ultra-stripped SNe rate and $R_{\rm DNS}$ constrained by future GW observations. This will help answer the question that, among the ultra-stripped SN and the dynamical formation channel, which one is the major path for forming DNS systems. to-do: fix this As such, further systematic searches for ultra-stripped SNe are requried to reduce the large uncertainties of the current estimation. Moving forward, the discovery of ultra-stripped SNe will still rely on high-cadence wide-field experiments such as ZTF. In particular, the upcoming ZTF-II, with a two-day cadence all sky survey, coupled with higher cadence boutique experiments, is well-positioned to carry out this task.

Acknowledgments

Software: astropy (Astropy Collaboration et al. 2013), corner (Foreman-Mackey 2016), CIGALE (Boquien et al. 2019), emcee (Foreman-Mackey et al. 2013), LAMBDAR (Wright et al. 2016), Lpipe (Perley 2019), matplotlib (Hunter 2007), pandas (McKinney 2010), pyneb (Luridiana et al. 2013), pyraf-dbsp (Bellm & Sesar 2016), scipy (Jones et al. 2001–), simsurvey (Feindt et al. 2019), sncosmo (Barbary et al. 2016)

Appendix A UV and Optical Data

Table 4. Optical and UV photometry for SN2019dge.

Date (JD)	Instrument	Filter	m	σ_m
58582.1544	LT+IOO	g	18.590	0.010
58582.1552	LT+IOO	r	18.840	0.020
58582.1575	LT+IOO	i	19.110	0.020
58582.1583	LT+IOO	z	19.280	0.070
58580.4421	P48+ZTF	g	20.828	0.148
58581.4807	P48+ZTF	g	18.813	0.033
58580.4842	P48+ZTF	r	20.891	0.139
58581.4308	P48+ZTF	r	19.187	0.050
58582.8289	*Swift*+UVOT	B	18.606	0.190
58582.8280	*Swift*+UVOT	U	18.289	0.110
58582.8346	*Swift*+UVOT	$UVM2$	18.550	0.070
58582.8261	*Swift*+UVOT	$UVW1$	18.685	0.110
58582.8299	*Swift*+UVOT	$UVW2$	18.802	0.100
58582.8337	*Swift*+UVOT	V	18.679	0.400

NOTE—m and σ_m are observed magnitude (without extinction correction) in AB system. A machine-readable table of all 117 photometric data points will be made available online.

Table 5. Photometry of the host galaxy

Instrument/Filter	$\lambda_{\rm eff}$ (Å)	m	σ_m
UVOT/$UVW2$	2079.0	20.492	0.124
UVOT/$UVM2$	2255.1	20.471	0.172
UVOT/$UVW1$	2614.2	20.081	0.155
UVOT/U	3475.5	19.631	0.145
UVOT/B	4359.1	18.812	0.139
UVOT/V	5430.1	18.194	0.171
SDSS/u'	3561.8	19.636	0.082
SDSS/g'	4718.9	18.540	0.015
SDSS/r'	6185.2	18.056	0.026
SDSS/i'	7499.7	17.885	0.028
SDSS/z'	8961.5	17.697	0.089
PS1/$g_{\rm PS1}$	4866.5	18.538	0.042
PS1/$r_{\rm PS1}$	6214.6	18.029	0.030
PS1/$i_{\rm PS1}$	7544.6	17.845	0.033
PS1/$z_{\rm PS1}$	8679.5	17.755	0.050
PS1/$y_{\rm PS1}$	9633.3	17.710	0.063
2MASS/J	12410.5	17.653	0.215
2MASS/H	16513.7	17.690	0.420
WISE/$W1$	34002.6	18.460	0.069
WISE/$W2$	46520.1	18.953	0.136

NOTE—m and σ_m are observed magnitude (without extinction correction) in the AB system.

The full set of photometry of SN2019dge is listed in Table 4. Photometry of the host galaxy SDSS J173646.73+503252.3 is listed in Table 5.
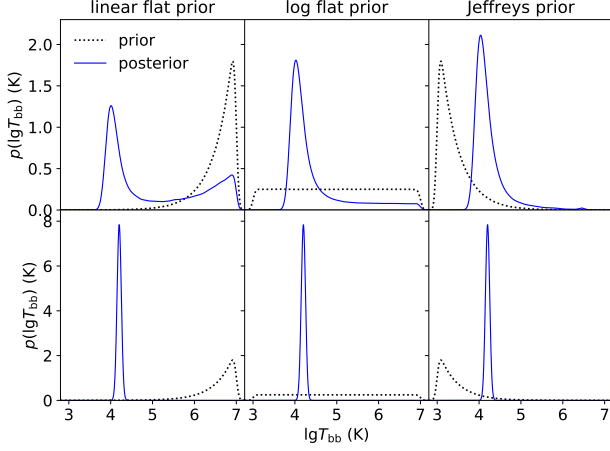
Figure B1. Posterior (solid lines) distribution of the black-body temperature $T_{\rm bb}$ on Apr 7 (upper panels) and Apr 9 (bottom panels) using three different priors (dotted lines).

Table 7. Shock cooling model parameters θ and their priors

θ	Description	Prior
$\log R_{\rm ext}$	$\log_{10}$ of extented material radius in cm	$\mathcal{U}(-5, 25)$
$\log M_{\rm ext}$	$\log_{10}$ of extented material mass in $M_\odot$	$\mathcal{U}(-4, 0)$
$t_{\rm exp}$	explosion epoch in MJD relative to 58583.2	$\mathcal{U}(-8, -2.76)$
E_{51}	SN energy divided by 10^{51} erg	$\mathcal{U}(0.01, 10)$
$E_{\rm ext,49}$	$E_{\rm ext}$ divided by 10^{49} erg	$\mathcal{U}(0.1, 100)$

Table 8. ^{56}Ni decay model parameters θ and their priors

θ	Description	Prior
$\tau_{\rm m}$	characteristic photon diffusion time in day	$\mathcal{U}(1, 20)$
$\log M_{\rm Ni}$	$\log_{10}$ of nickel mass in $M_\odot$	$\mathcal{U}(-4, 0)$
t_0	characteristic γ-ray escape time in day	$\mathcal{U}(20, 100)$

Table 6. Physical evolution of SN2019dge from blackbody fits.

Δt	$L(10^{41}\,{\rm erg\,s^{-1}})$	$R\ (10^3\ R_\odot)$	$T\ (10^3\ {\rm K})$
-2.74	$2.98^{+578.84}_{-1.41}$	$1.45^{+1.14}_{-1.14}$	$14.21^{+101.35}_{-5.12}$
-1.72	$44.63^{+43.85}_{-15.84}$	$2.20^{+0.44}_{-0.46}$	$22.75^{+7.60}_{-4.14}$
-0.66	$27.15^{+1.13}_{-1.07}$	$3.48^{+0.08}_{-0.08}$	$15.96^{+0.34}_{-0.33}$
0.27	$19.26^{+0.77}_{-0.72}$	$4.92^{+0.14}_{-0.14}$	$12.32^{+0.29}_{-0.28}$
1.10	$15.72^{+0.46}_{-0.42}$	$5.39^{+0.14}_{-0.14}$	$11.20^{+0.23}_{-0.22}$
3.26	$8.34^{+0.22}_{-0.20}$	$7.26^{+0.46}_{-0.44}$	$8.23^{+0.31}_{-0.28}$
4.24	$7.29^{+0.26}_{-0.22}$	$7.38^{+0.88}_{-0.83}$	$7.88^{+0.54}_{-0.46}$
5.25	$6.10^{+0.16}_{-0.15}$	$8.77^{+0.78}_{-0.73}$	$6.92^{+0.33}_{-0.30}$
6.83	$6.18^{+0.63}_{-0.46}$	$7.09^{+1.01}_{-0.92}$	$7.72^{+0.75}_{-0.62}$
7.98	$5.29^{+0.24}_{-0.21}$	$8.00^{+0.75}_{-0.70}$	$6.99^{+0.39}_{-0.35}$
8.98	$5.49^{+0.44}_{-0.36}$	$6.79^{+0.94}_{-0.85}$	$7.66^{+0.65}_{-0.56}$
10.05	$4.55^{+0.37}_{-0.27}$	$7.42^{+1.03}_{-0.96}$	$6.99^{+0.63}_{-0.52}$
10.92	$4.49^{+0.64}_{-0.44}$	$6.63^{+1.25}_{-1.06}$	$7.37^{+0.93}_{-0.75}$
11.89	$4.04^{+0.24}_{-0.21}$	$7.42^{+0.83}_{-0.75}$	$6.79^{+0.45}_{-0.40}$
13.06	$3.34^{+0.10}_{-0.10}$	$7.52^{+0.69}_{-0.66}$	$6.43^{+0.32}_{-0.29}$
14.05	$3.08^{+0.10}_{-0.09}$	$7.05^{+0.63}_{-0.59}$	$6.51^{+0.32}_{-0.29}$
14.97	$2.82^{+0.15}_{-0.12}$	$7.30^{+1.21}_{-1.06}$	$6.25^{+0.57}_{-0.49}$
16.09	$2.45^{+0.09}_{-0.09}$	$6.17^{+0.59}_{-0.58}$	$6.56^{+0.33}_{-0.29}$
23.96	$1.02^{+0.07}_{-0.06}$	$5.47^{+1.23}_{-1.12}$	$5.59^{+0.74}_{-0.54}$
27.00	$0.72^{+0.08}_{-0.08}$	$4.08^{+1.26}_{-1.01}$	$5.93^{+0.91}_{-0.70}$
27.98	$0.78^{+0.07}_{-0.06}$	$5.73^{+1.68}_{-1.29}$	$5.10^{+0.68}_{-0.57}$
29.23	$0.83^{+0.11}_{-0.09}$	$4.76^{+2.47}_{-1.56}$	$5.64^{+1.23}_{-0.93}$
33.24	$1.09^{+0.16}_{-0.11}$	$6.99^{+2.47}_{-1.74}$	$5.02^{+0.65}_{-0.56}$

Appendix B Modeling of SN2019dge

B.1 Modeling the Physical Evolution

To model the multi-band light curve with a black-body function, we utilized the Monte Carlo Markov Chain (MCMC) simulations with emcee (Foreman-Mackey et al. 2013). We test the performance of three types of model priors for the blackbody radius ($R_{\rm bb}$) and temperature ($T_{\rm bb}$): (i) $T_{\rm bb}$ and $R_{\rm bb}$ are uniformly distributed in the range of $[10^3,\ 10^7]$ K and $[10,\ 10^6]\ R_\odot$, respectively (ii) the two parameters are logarithmically uniformly distributed in the same ranges (ii) the two parameters follow Jeffreys prior (Jeffreys 1946) in the same ranges.

Within the ensemble, we use 100 walkers, each of which is run until convergence or 100,000 steps, whichever comes first. The test for convergence follows steps outlined in Yao et al. (2019) and Miller et al. (2020). We adopt the 68% credible region (i.e., 16$^{\rm th}$ and 84$^{\rm th}$ percentiles of posterior probability distributions) as the model uncertainties quoted in Table 6.

We examine the fitting results under different choices of priors in Figure B1, which shows the posterior distribution of $T_{\rm bb}$ using data obtained on Apr 7 (top panels) and Apr 9 (bottom panels). Early stages of SN evolution often feature extremely high temperatures. At an epoch where both UV and optical data are available (Apr 9), the posterior does not depend on the particular choice of prior, and the model parameter can thus be well constrained. However, at our first detection epoch where only optical data is available (Apr 7), the posterior strongly depends on the prior. For a linearly flat prior, high numbers receive a lot of "weight",
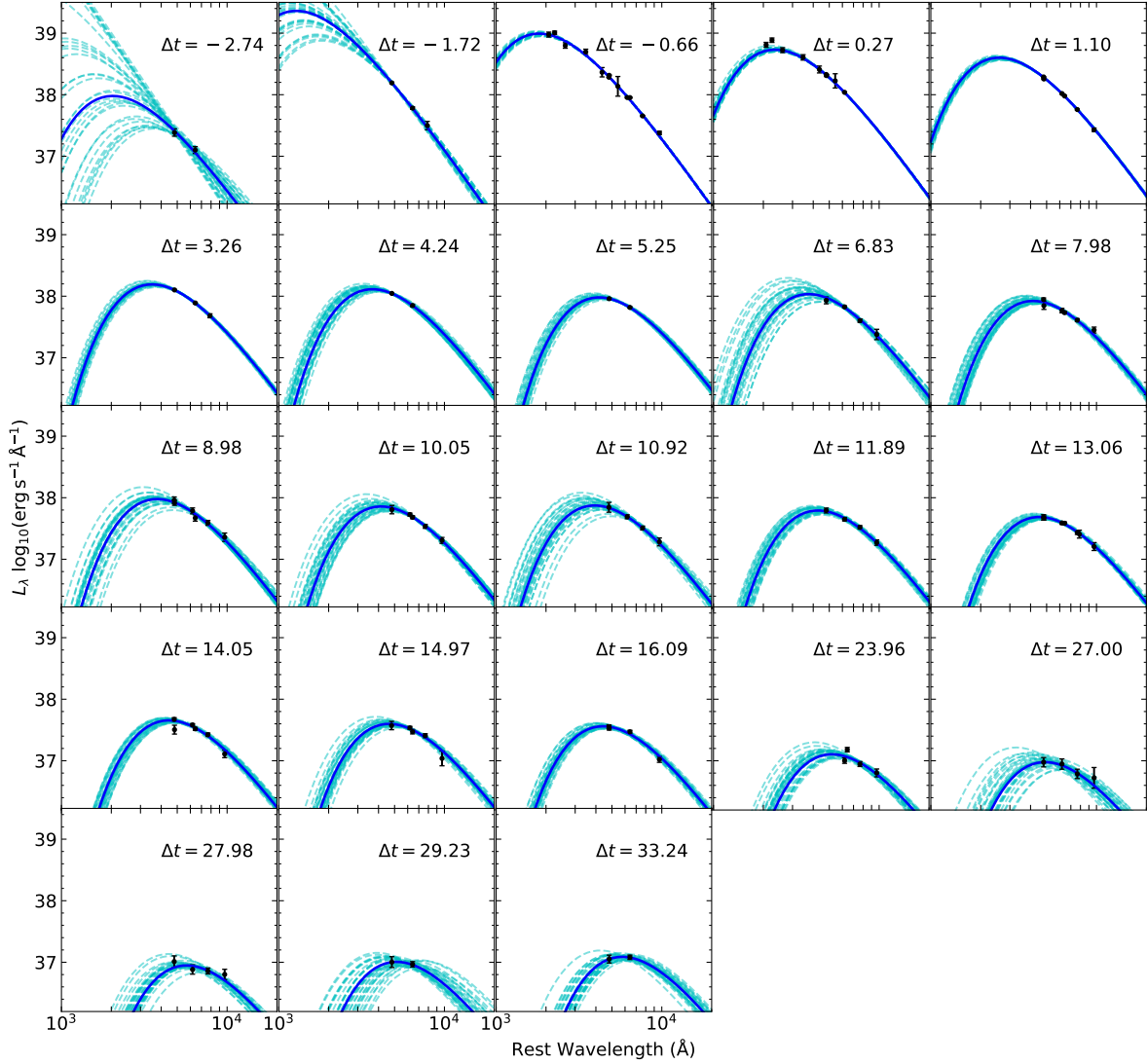
Figure B2. Black data points are *Swift*/UVOT and optical photometry of SN2019dge. Solid lines show model fits using estimated parameters, while 30 random draws from the MCMC posterior are shown with dashed lines.

making the "multi-peaks" shape posterior in the upper left panel of Figure B1. Log prior and Jeffreys prior generally give the same result. Given that all models were run to converge using the log prior, whereas fitting of the first epoch did not converge adopting Jeffreys prior, we adopt results using log prior in this study.

In Figure B2 we show the photometry interpolated onto common epochs, and fit to a blackbody function to derive the photospheric evolution. The resulting evolution in bolometric lumonosity, photospheric radius, and effective temperatures is listed in Table 6.

B.2 Modeling Early Light Curve

We cast the P15 analytical expression for the shape of the early-time light curve in terms of M_{ext}, R_{ext}, E_{ext},

and E_{51}:

$$L(t) = \frac{t_e E_{\mathrm{ext}}}{t_p^2} \exp\left[-\frac{t(t + 2t_e)}{2t_p^2}\right] \, \mathrm{erg\,s^{-1}} \qquad \text{(B1a)}$$

$$t_e = 10^{-9} R_{\mathrm{ext}} E_{\mathrm{ext},49}^{-1/2} \left(\frac{M_{\mathrm{ext}}}{0.01 M_\odot}\right)^{1/2} \, \mathrm{s} \qquad \text{(B1b)}$$

$$t_p = 1.1 \times 10^5 \kappa_{0.34}^{1/2} E_{51}^{-0.01/1.4}$$

$$\times E_{\mathrm{ext},49}^{-0.17/0.7} \left(\frac{M_{\mathrm{ext}}}{0.01 M_\odot}\right)^{0.74} \, \mathrm{s} \qquad \text{(B1c)}$$

where t is time since explosion in seconds, $\kappa_{0.34} = \kappa/(0.34\,\mathrm{cm^2\,g^{-1}})$, $E_{\mathrm{ext},49} = E_{\mathrm{ext}}/(10^{49}\,\mathrm{erg})$, $E_{51} = E/(10^{51}\,\mathrm{erg})$, and E is energy of the explosion.Following
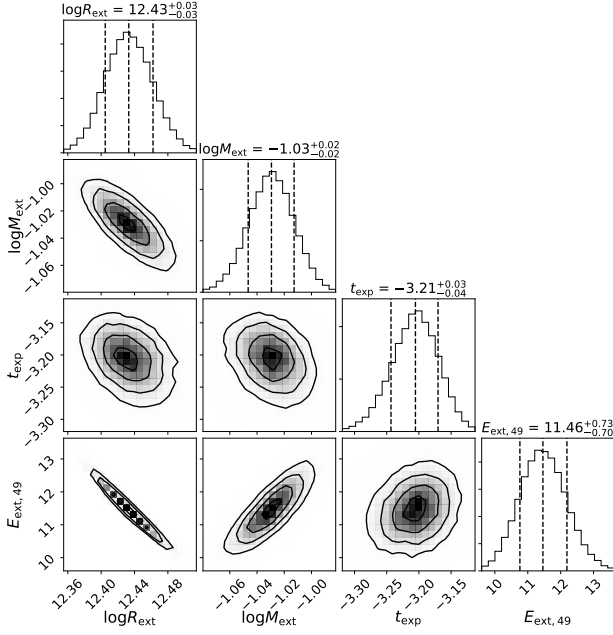
Figure B3. Corner plot showing the posterior constraints on $\log R_{\rm ext}$, $\log M_{\rm ext}$, $t_{\rm fl}$, and $E_{\rm ext,49}$. Marginalized one-dimensional distributions are shown along the diagonal, along with the median estimate and the 68% credible region (shown with vertical dashed lines).
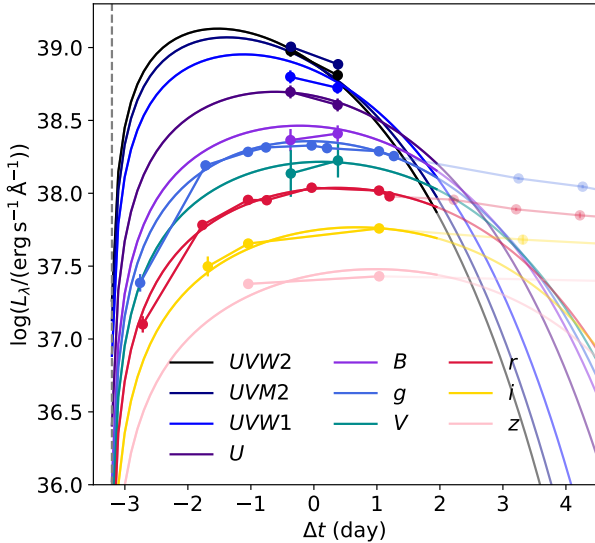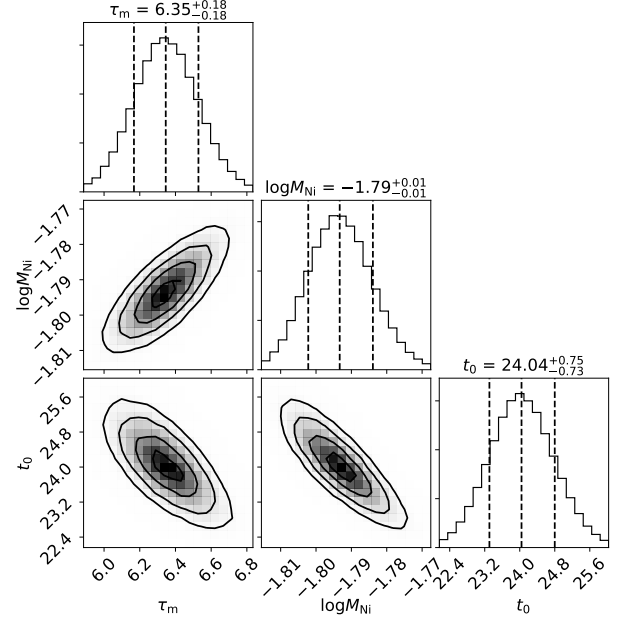

Figure B5. Corner plot showing the posterior constraints on $\tau_{\rm m}$, $\log M_{\rm Ni}$, and t_0. Marginalized one-dimensional distributions are shown along the diagonal, along with the median estimate and the 68% credible region (shown with vertical dashed lines).

P15 we assume the emission is a blackbody at radius

$$R(t) = R_{\rm ext} + 10^9 \left(\frac{E_{\rm ext}}{10^{49}\,{\rm erg\,s^{-1}}} \right)^{1/2} \left(\frac{M_{\rm ext}}{0.01 M_\odot} \right)^{-0.5} t \tag{B2}$$

and temperature

$$T(t) = \left(\frac{L(t)}{4\pi R(t)^2 \sigma_{\rm SB}} \right)^{1/4} \tag{B3}$$

We fix $\kappa \approx 0.2\,{\rm cm^2\,g^{-1}}$ as appropriate for a hydrogen-deficient ionized gas, and assign wide flat priors for all model parameters, as summarized in Table 7. We only include observations up to $\Delta t = 2\,{\rm d}$ in the fitting. We found that this particular choice of Δt — 2 d instead of 1 d or 3 d — in general does not affect the final inference for the model parameters. Figure B3 shows the corner plot of $\log R_{\rm ext}$, $\log M_{\rm ext}$, $t_{\rm fl}$, and $E_{\rm ext,49}$. For clarity, E_{51} is excluded as it does not exhibit strong covariance with the parameters shown here. This can be understood by Eq. B1c, which gives $t_p \propto E_{51}^{-0.01/1.4}$, suggesting that the shock cooling luminosity only weakly depends on E_{51}.

The maximum a posteriori model is visualized by solid lines in Figure B4 color-coded in different filters. The rising part of the model does not closely match to data due to the ignorance of the density structure of the stel-

Figure B4. Cooling emission model fit to the early light curve of SN2019dge. Data excluded from the fitting are shown as transparent circles. The maximum a posteriori model is shown via solid lines. The vertical dashed line shows the median 1-D marginalized posterior value of $t_{\rm fl}$.

lar profile. Nevertheless, the peak of the light curve is well captured by this model.
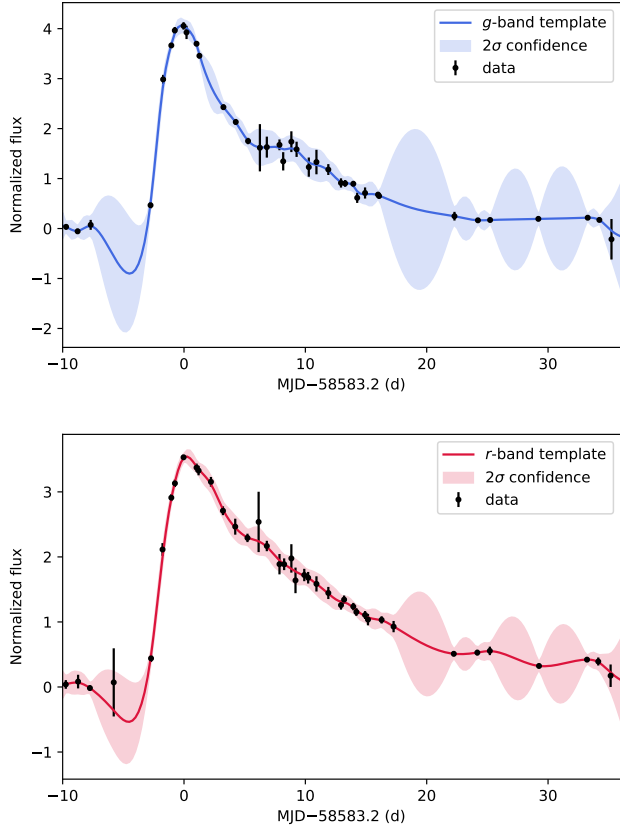

Figure B6. *g-* and *r-*band light curve templates for SN2019dge obtained from Gaussian process fitting.

B.3 Modeling the Main Peak

to-do: radioactive decay give both gamma-rays and positrons

For ^{56}Ni$\rightarrow^{56}$Co$\rightarrow^{56}$Fe decay powered explosions, the energy deposition rate is

$$\varepsilon_{\mathrm{rad}} = \varepsilon_{\mathrm{Ni},\gamma}(t) + \varepsilon_{\mathrm{Co},\gamma}(t) \tag{B4}$$

$$\varepsilon_{\mathrm{Ni},\gamma}(t) = \epsilon_{\mathrm{Ni}}e^{-t/\tau_{\mathrm{Ni}}} \tag{B5}$$

$$\varepsilon_{\mathrm{Co},\gamma}(t) = \epsilon_{\mathrm{Co}}\left(e^{-t/\tau_{\mathrm{Co}}} - e^{-t/\tau_{\mathrm{Ni}}}\right) \tag{B6}$$

where $\epsilon_{\mathrm{Ni}} = 3.90 \times 10^{10}\,\mathrm{erg\,g^{-1}\,s^{-1}}$, $\epsilon_{\mathrm{Co}} = 6.78 \times 10^{9}\,\mathrm{erg\,g^{-1}\,s^{-1}}$, $\tau_{\mathrm{Ni}} = 8.8\,\mathrm{d}$ and $\tau_{\mathrm{Co}} = 111.3\,\mathrm{d}$ are the decay lifetimes of ^{56}Ni and ^{56}Co (Nadyozhin 1994). The effective heating rate is modified by the probability of thermalization, and thus $\varepsilon_{\mathrm{heat}} \leq \varepsilon_{\mathrm{rad}}$.

The bolometric light curve can be generally divided into the photospheric phase and the nebular phase. The photospheric phase can be modelled using Equations given in Valenti et al. (2008, Appendix A), with modifications given by Lyman et al. (2016, Eq. 3),

$$
\begin{aligned}
L_{\mathrm{phot}}(t) = &M_{\mathrm{Ni}}e^{-x^2} \times \\
&\left[(\epsilon_{\mathrm{Ni}} - \epsilon_{\mathrm{Co}}) \int_0^x (2ze^{-2zy+z^2})\mathrm{d}z \right. \\
&\left. + \epsilon_{\mathrm{Co}} \int_0^x (2ze^{-2zy+2zs+z^2})\mathrm{d}z \right]
\end{aligned} \tag{B7}
$$

where $x = t/\tau_{\mathrm{m}}$, $y = \tau_{\mathrm{m}}/(2\tau_{\mathrm{Ni}})$,

$$s = \frac{\tau_{\mathrm{m}}(\tau_{\mathrm{Co}} - \tau_{\mathrm{Ni}})}{2\tau_{\mathrm{Co}}\tau_{\mathrm{Ni}}}, \tag{B8}$$

$$\tau_{\mathrm{m}} = \left(\frac{2\kappa_{\mathrm{opt}}M_{\mathrm{ej}}}{13.8cv_{\mathrm{phot}}}\right)^{1/2} \tag{B9}$$

In the nebular phase the SN ejecta become optically thin, such that the delay between the energy deposition from radioactivity and the optical radiation becomes shorter. The bolometric luminosity is then equal to the rate of energy deposition: $L_{\mathrm{neb}}(t) = Q(t)$. At any given time, the energy deposition rate $Q(t)$ is (Wheeler et al. 2015; Wygoda et al. 2019):

$$Q(t) \approx Q_{\gamma}(t)\left(1 - e^{-(t_0/t)^2}\right) \tag{B10}$$

where $Q_{\gamma}(t) = M_{\mathrm{Ni}}\varepsilon_{\mathrm{rad}}$ is the energy release rate of gamma-raysto-do: on the spot??, t_0 is the time at which the ejecta becomes optically thin to gamma rays. Here the difference between energy deposition rate of gamma-rays and positrons is neglected.

to-do: add motivation to say that this is ok To fit the shock cooling subtracted bolometric light curve with a simple radioactive decay model, we do not divide the data into photospheric phase and nebular phase, but instead adopt the following formula for the whole light curve:

$$L(t) = L_{\mathrm{phot}}(t)\left(1 - e^{-(t_0/t)^2}\right) \tag{B11}$$

Priors or the model parameters are summarized in Table 8, and Figure B5 shows the corner plot of τ_{m}, $\log M_{\mathrm{Ni}}$, and t_0.

B.4 Generating a Light Curve Template for SN2019dge

To construct a template for SN2019dge in the ZTF g and r filters, we model the observed light curve by a Gaussian process. We denote the measurements as $(\mathbf{x}, \mathbf{y})$, where $\mathbf{x}$ is MJD-58583.2, and $\mathbf{y}$ is flux calculated as $10^{-0.4m} \times 10^8$ (m is magnitude). We choose a kernel in the form of Matern covariance function (Rasmussen

2003, Eq. 4.17):

$$k_{3/2}(x, x') = A \left(1 + \frac{\sqrt{3}r}{l}\right) \exp\left(-\frac{\sqrt{3}r}{l}\right) \quad \text{(B12)}$$

where $r = |x - x'|$. A and r in Eq. B12 are chosen to minimize the negative log likelihood function (see, e.g., Eq. 2.43 of Rasmussen 2003).

We perform the fit from $x = -10\,\mathrm{d}$ to $x = +40\,\mathrm{d}$, and the obtained templates are shown in Figure B6.

References

Abbott, B. P., Abbott, R., Abbott, T. D., et al. 2020, ApJL, 892, L3

—. 2017a, Physical Review Letters, 119, 161101

—. 2017b, ApJL, 848, L12

Ahn, C. P., Alexandroff, R., Allende Prieto, C., et al. 2012, ApJS, 203, 21

Alam, S., Albareti, F. D., Allende Prieto, C., et al. 2015, ApJS, 219, 12

Andrews, J. J., & Mandel, I. 2019, ApJL, 880, L8

Arnett, W. D. 1982, ApJ, 253, 785

Asplund, M., Grevesse, N., Sauval, A. J., & Scott, P. 2009, ARA&A, 47, 481

Astropy Collaboration, Robitaille, T. P., Tollerud, E. J., et al. 2013, A&A, 558, A33

Barbary, K., Barclay, T., Biswas, R., et al. 2016, SNCosmo: Python library for supernova cosmology

Barnsley, R. M., Smith, R. J., & Steele, I. A. 2012, AN, 333, 101

Bellm, E. C., & Sesar, B. 2016, pyraf-dbsp: Reduction pipeline for the Palomar Double Beam Spectrograph

Bellm, E. C., Kulkarni, S. R., Graham, M. J., et al. 2019a, PASP, 131, 018002

Bellm, E. C., Kulkarni, S. R., Barlow, T., et al. 2019b, PASP, 131, 068003

Boquien, M., Burgarella, D., Roehlly, Y., et al. 2019, A&A, 622, A103

Bray, J. C., & Eldridge, J. J. 2016, MNRAS, 461, 3747

Bruzual, G., & Charlot, S. 2003, MNRAS, 344, 1000

Bufano, F., Immler, S., Turatto, M., et al. 2009, ApJ, 700, 1456

Burrows, D. N., Hill, J. E., Nousek, J. A., et al. 2005, SSRv, 120, 165

Calzetti, D., Armus, L., Bohlin, R. C., et al. 2000, ApJ, 533, 682

Cardelli, J. A., Clayton, G. C., & Mathis, J. S. 1989, ApJ, 345, 245

Chabrier, G. 2003, PASP, 115, 763

Charlot, S., & Fall, S. M. 2000, ApJ, 539, 718

Chen, P., Dong, S., Stritzinger, M. D., et al. 2020, ApJL, 889, L6

Chevalier, R. A. 1982, ApJ, 259, 302

—. 1998, ApJ, 499, 810

Chugai, N. N., & Danziger, I. J. 1994, MNRAS, 268, 173

Coulter, D. A., Foley, R. J., Kilpatrick, C. D., et al. 2017, Science, 358, 1556

De, K., Kasliwal, M. M., Cantwell, T., et al. 2018a, ApJ, 866, 72

De, K., Kasliwal, M. M., Ofek, E. O., et al. 2018b, Science, 362, 201

De, K., Kasliwal, M. M., Tzanidakis, A., et al. 2020a, arXiv, arXiv:2004.09029

De, K., Hankins, M. J., Kasliwal, M. M., et al. 2020b, PASP, 132, 025001

Dekany, R., Smith, R. M., Riddle, R., et al. 2020, Publications of the Astronomical Society of the Pacific, 132, 038001

Dessart, L., Hillier, D. J., Li, C., & Woosley, S. 2012, MNRAS, 424, 2139

Dewi, J. D. M., Pols, O. R., Savonije, G. J., & van den Heuvel, E. P. J. 2002, MNRAS, 331, 1027

Dey, A., Schlegel, D. J., Lang, D., et al. 2019, AJ, 157, 168

Draine, B. T., & Li, A. 2007, ApJ, 657, 810

Drout, M. R., Soderberg, A. M., Gal-Yam, A., et al. 2011, ApJ, 741, 97

Drout, M. R., Soderberg, A. M., Mazzali, P. A., et al. 2013, ApJ, 774, 58

East, W. E., & Pretorius, F. 2012, ApJL, 760, L4

Eldridge, J. J., Fraser, M., Smartt, S. J., et al. 2013, MNRAS, 436, 774

Feindt, U., Nordin, J., Rigault, M., et al. 2019, JCAP, 2019, 005

Filippenko, A. V. 1997, ARA&A, 35, 309

Flewelling, H. A., Magnier, E. A., Chambers, K. C., et al. 2016

Foreman-Mackey, D. 2016, JOSS, 24

Foreman-Mackey, D., Hogg, D. W., Lang, D., & Goodman, J. 2013, PASP, 125, 306

Fransson, C., Benvenuti, P., Gordon, C., et al. 1984, A&A, 132, 1

Fremling, C., Sollerman, J., Taddia, F., et al. 2016, A&A, 593, A68

Fremling, C., Sollerman, J., Kasliwal, M. M., et al. 2018, A&A, 618, A37

Fremling, C., Ko, H., Dugas, A., et al. 2019a, ApJL, 878, L5

Fremling, U. C., Miller, A. A., Sharma, Y., et al. 2019b, arXiv, arXiv:1910.12973

Fruchter, A. S. 2018, A New Approach to Following Transients with HST: Rolling Snapshots, HST Proposal, HST Proposal

Gal-Yam, A. 2017, Observational and Physical Classification of Supernovae, ed. A. W. Alsabti & P. Murdin, 195

Gal-Yam, A., Bufano, F., Barlow, T. A., et al. 2008, ApJL, 685, L117

Gal-Yam, A., Arcavi, I., Ofek, E. O., et al. 2014, Nature, 509, 471

Gehrels, N., Chincarini, G., Giommi, P., et al. 2004, ApJ, 611, 1005

Goldstein, A., Veres, P., Burns, E., et al. 2017, ApJL, 848, L14

Graham, M. J., Kulkarni, S. R., Bellm, E. C., et al. 2019, PASP, 131, 078001

Guillochon, J., Parrent, J., Kelley, L. Z., & Margutti, R. 2017, ApJ, 835, 64

Hachinger, S., Mazzali, P. A., Taubenberger, S., et al. 2012, MNRAS, 422, 70

Hallinan, G., Corsi, A., Mooley, K. P., et al. 2017, Science, 358, 1579

Hamuy, M., Maza, J., Pinto, P. A., et al. 2002, AJ, 124, 417

HEASARC. 2014, HEAsoft: Unified Release of FTOOLS and XANADU, Astrophysics Source Code Library, ascl, ascl

Hijikawa, K., Kinugawa, T., Yoshida, T., & Umeda, H. 2019, ApJ, 882, 93

Ho, A. Y. Q., Phinney, E. S., Ravi, V., et al. 2019a, ApJ, 871, 73

Ho, A. Y. Q., Goldstein, D. A., Schulze, S., et al. 2019b, ApJ, 887, 169

Ho, A. Y. Q., Perley, D. A., Kulkarni, S. R., et al. 2020, arXiv, arXiv:2003.01222

Ho, P. T. P., Moran, J. M., & Lo, K. Y. 2004, ApJL, 616, L1

Horesh, A., Stockdale, C., Fox, D. B., et al. 2013, MNRAS, 436, 1258

Hosseinzadeh, G., Arcavi, I., Valenti, S., et al. 2017, ApJ, 836, 158

Huang, C., & Chevalier, R. A. 2018, MNRAS, 475, 1261

Hunter, J. D. 2007, Computing In Science & Engineering, 9, 90

Jacobson-Galán, W. V., Margutti, R., Kilpatrick, C. D., et al. 2020, arXiv, arXiv:2005.01782

Jeffery, D. J., Kirshner, R. P., Challis, P. M., et al. 1994, ApJL, 421, L27

Jeffreys, H. 1946, Proceedings of the Royal Society of London. Series A. Mathematical and Physical Sciences, 186, 453

Jones, E., Oliphant, T., Peterson, P., et al. 2001–, SciPy: Open source scientific tools for Python

Kasen, D. 2017, Unusual Supernovae and Alternative Power Sources, ed. A. W. Alsabti & P. Murdin, 939

Kasliwal, M. M., Kulkarni, S. R., Gal-Yam, A., et al. 2010, ApJL, 723, L98

—. 2012, ApJ, 755, 161

Kasliwal, M. M., Nakar, E., Singer, L. P., et al. 2017, Science, 358, 1559

Kasliwal, M. M., Cannella, C., Bagdasaryan, A., et al. 2019, PASP, 131, 038003

Kennicutt, Robert C., J. 1998, ApJ, 498, 541

Khatami, D. K., & Kasen, D. N. 2019, ApJ, 878, 56

Khazov, D., Yaron, O., Gal-Yam, A., et al. 2016, ApJ, 818, 3

Kingdon, J., Ferland, G. J., & Feibelman, W. A. 1995, ApJ, 439, 793

Kleiser, I., Fuller, J., & Kasen, D. 2018a, MNRAS, 481, L141

Kleiser, I. K. W., & Kasen, D. 2014, MNRAS, 438, 318

Kleiser, I. K. W., Kasen, D., & Duffell, P. C. 2018b, MNRAS, 475, 3152

Komatsu, E., Smith, K. M., Dunkley, J., et al. 2011, ApJS, 192, 18

Kroupa, P. 2001, MNRAS, 322, 231

Lang, D. 2014, AJ, 147, 108

Laplace, E., Götberg, Y., de Mink, S. E., et al. 2020, arXiv, arXiv:2003.01120

Law, N. M., Kulkarni, S. R., Dekany, R. G., et al. 2009, PASP, 121, 1395

Leibundgut, B., Kirshner, R. P., Pinto, P. A., et al. 1991, ApJ, 372, 531

Li, H., & McCray, R. 1992, ApJ, 387, 309

Li, W., Chornock, R., Leaman, J., et al. 2011a, MNRAS, 412, 1473

Li, W., Leaman, J., Chornock, R., et al. 2011b, MNRAS, 412, 1441

Liu, Y.-Q., Modjaz, M., Bianco, F. B., & Graur, O. 2016, ApJ, 827, 90

Luridiana, V., Morisset, C., & Shaw, R. A. 2013, PyNeb: Analysis of emission lines

Lyman, J. D., Bersier, D., James, P. A., et al. 2016, MNRAS, 457, 328

Madau, P., & Dickinson, M. 2014, ARA&A, 52, 415

Margutti, R., Metzger, B. D., Chornock, R., et al. 2019, ApJ, 872, 18

Marino, R. A., Rosales-Ortega, F. F., Sánchez, S. F., et al. 2013, A&A, 559, A114

Masci, F. J., Laher, R. R., Rusholme, B., et al. 2019, PASP, 131, 018003

Mazzali, P. A., Sullivan, M., Hachinger, S., et al. 2014, MNRAS, 439, 1959

McBrien, O. R., Smartt, S. J., Chen, T.-W., et al. 2019, ApJL, 885, L23

McKinney, W. 2010, 51

Meisner, A. M., Lang, D., & Schlegel, D. J. 2017, AJ, 153, 38

Miller, A. A., Yao, Y., Bulla, M., et al. 2020, arXiv, arXiv:2001.00598

Modjaz, M., Gutiérrez, C. P., & Arcavi, I. 2019, NatAs, 3, 717

Modjaz, M., Bianco, F. B., Siwek, M., et al. 2020, ApJ, 892, 153

Moriya, T., Tominaga, N., Tanaka, M., et al. 2010, ApJ, 719, 1445

Moriya, T. J., Tominaga, N., Langer, N., et al. 2014, A&A, 569, A57

Moriya, T. J., Mazzali, P. A., Tominaga, N., et al. 2017, MNRAS, 466, 2085

Müller, B., Gay, D. W., Heger, A., et al. 2018, MNRAS, 479, 3675

Nadyozhin, D. K. 1994, ApJS, 92, 527

Nakaoka, T., Maeda, K., Yamanaka, M., et al. 2020, arXiv, arXiv:2005.02992

Nakar, E., & Piro, A. L. 2014, ApJ, 788, 193

Nomoto, K., Yamaoka, H., Pols, O. R., et al. 1994, Nature, 371, 227

Ofek, E. O., Lin, L., Kouveliotou, C., et al. 2013a, ApJ, 768, 47

Ofek, E. O., Fox, D., Cenko, S. B., et al. 2013b, ApJ, 763, 42

Oke, J. B., & Gunn, J. E. 1982, PASP, 94, 586

Oke, J. B., Cohen, J. G., Carr, M., et al. 1995, PASP, 107, 375

Panagia, N., Vettolani, G., Boksenberg, A., et al. 1980, MNRAS, 192, 861

Pastorello, A., Mattila, S., Zampieri, L., et al. 2008, MNRAS, 389, 113

Pastorello, A., Benetti, S., Brown, P. J., et al. 2015, MNRAS, 449, 1921

Patterson, M. T., Bellm, E. C., Rusholme, B., et al. 2019, PASP, 131, 018001

Peimbert, M., Peimbert, A., & Delgado-Inglada, G. 2017, PASP, 129, 082001

Peimbert, M., Peimbert, A., & Ruiz, M. T. 2000, ApJ, 541, 688

Perley, D. A. 2019, PASP, 131, 084503

Perley, D. A., Mazzali, P. A., Yan, L., et al. 2019, MNRAS, 484, 1031

Pettini, M., & Pagel, B. E. J. 2004, MNRAS, 348, L59

Piascik, A. S., Steele, I. A., Bates, S. D., et al. 2014, Society of Photo-Optical Instrumentation Engineers (SPIE) Conference Series, Vol. 9147, SPRAT: Spectrograph for the Rapid Acquisition of Transients, 91478H

Piro, A. L. 2015, ApJL, 808, L51

Piro, A. L., & Morozova, V. S. 2014, ApJL, 792, L11

Polin, A., Nugent, P., & Kasen, D. 2019, ApJ, 873, 84

Poznanski, D., Chornock, R., Nugent, P. E., et al. 2010, Science, 327, 58

Prentice, S. J., Maguire, K., Smartt, S. J., et al. 2018, ApJL, 865, L3

Prentice, S. J., Ashall, C., James, P. A., et al. 2019, MNRAS, 485, 1559

Quataert, E., & Shiode, J. 2012, MNRAS, 423, L92

Rasmussen, C. E. 2003, Springer, 63

Rau, A., Kulkarni, S. R., Law, N. M., et al. 2009, PASP, 121, 1334

Rest, A., Garnavich, P. M., Khatami, D., et al. 2018, NatAs, 2, 307

Roming, P. W. A., Kennedy, T. E., Mason, K. O., et al. 2005, SSRv, 120, 95

Sanders, N. E., Soderberg, A. M., Levesque, E. M., et al. 2012, ApJ, 758, 132

Schlafly, E. F., & Finkbeiner, D. P. 2011, ApJ, 737, 103

Schlegel, D. J., Finkbeiner, D. P., & Davis, M. 1998, ApJ, 500, 525

Shen, K. J., Kasen, D., Weinberg, N. N., et al. 2010, ApJ, 715, 767

Shivvers, I., Zheng, W., Van Dyk, S. D., et al. 2017, MNRAS, 471, 4381

Shivvers, I., Filippenko, A. V., Silverman, J. M., et al. 2019, MNRAS, 482, 1545

Sim, S. A., Fink, M., Kromer, M., et al. 2012, MNRAS, 420, 3003

Skrutskie, M. F., Cutri, R. M., Stiening, R., et al. 2006, AJ, 131, 1163

Smith, N. 2014, ARA&A, 52, 487

—. 2017, Interacting Supernovae: Types IIn and Ibn, ed. A. W. Alsabti & P. Murdin, 403

Smith, N., Li, W., Filippenko, A. V., & Chornock, R. 2011, MNRAS, 412, 1522

Smith, N., Mauerhan, J. C., Cenko, S. B., et al. 2015, MNRAS, 449, 1876

Steele, I. A., Smith, R. J., Rees, P. C., et al. 2004, Proc. SPIE, 5489, 679

Storey, P. J., & Hummer, D. G. 1995, MNRAS, 272, 41

Sullivan, M., Kasliwal, M. M., Nugent, P. E., et al. 2011, ApJ, 732, 118

Suwa, Y., Yoshida, T., Shibata, M., et al. 2015, MNRAS, 454, 3073

Taddia, F., Stritzinger, M. D., Bersten, M., et al. 2018, A&A, 609, A136

Tauris, T. M., Langer, N., & Kramer, M. 2012, MNRAS, 425, 1601

Tauris, T. M., Langer, N., Moriya, T. J., et al. 2013, ApJL, 778, L23

Tauris, T. M., Langer, N., & Podsiadlowski, P. 2015, MNRAS, 451, 2123

Tauris, T. M., Kramer, M., Freire, P. C. C., et al. 2017, ApJ, 846, 170

Valenti, S., Benetti, S., Cappellaro, E., et al. 2008, MNRAS, 383, 1485

Weiler, K. W., Williams, C. L., Panagia, N., et al. 2007, ApJ, 671, 1959

Wellons, S., Soderberg, A. M., & Chevalier, R. A. 2012, ApJ, 752, 17

Wheeler, J. C., Johnson, V., & Clocchiatti, A. 2015, MNRAS, 450, 1295

Whitesides, L., Lunnan, R., Kasliwal, M. M., et al. 2017, ApJ, 851, 107

Willingale, R., Starling, R. L. C., Beardmore, A. P., et al. 2013, MNRAS, 431, 394

Woosley, S. E. 2019, ApJ, 878, 49

Wright, A. H., Robotham, A. S. G., Bourne, N., et al. 2016, MNRAS, 460, 765

Wygoda, N., Elbaz, Y., & Katz, B. 2019, MNRAS, 484, 3951

Yan, L., Quimby, R., Gal-Yam, A., et al. 2017, ApJ, 840, 57

Yao, Y., Miller, A. A., Kulkarni, S. R., et al. 2019, ApJ, 886, 152

Yaron, O., & Gal-Yam, A. 2012, PASP, 124, 668

Yaron, O., Perley, D. A., Gal-Yam, A., et al. 2017, Nature Physics, 13, 510

Yoon, S. C., Woosley, S. E., & Langer, N. 2010, ApJ, 725, 940

Zackay, B., Ofek, E. O., & Gal-Yam, A. 2016, ApJ, 830, 27

Zapartas, E., de Mink, S. E., Van Dyk, S. D., et al. 2017, ApJ, 842, 125